ARTICLE

The lectin Discoidin I acts in the cytoplasm to help assemble the contractile machinery

Ly T.S. Nguyen[1] and Douglas N. Robinson[1]

Cellular functions, such as division and migration, require cells to undergo robust shape changes. Through their contractility machinery, cells also sense, respond, and adapt to their physical surroundings. In the cytoplasm, the contractility machinery organizes into higher order assemblies termed contractility kits (CKs). Using *Dictyostelium discoideum*, we previously identified Discoidin I (DscI), a classic secreted lectin, as a CK component through its physical interactions with the actin crosslinker Cortexillin I (CortI) and the scaffolding protein IQGAP2. Here, we find that DscI ensures robust cytokinesis through regulating intracellular components of the contractile machinery. Specifically, DscI is necessary for normal cytokinesis, cortical tension, membrane–cortex connections, and cortical distribution and mechanoresponsiveness of CortI. The *dscI* deletion mutants also have complex genetic epistatic relationships with CK components, acting as a genetic suppressor of *cortI* and *iqgap1*, but as an enhancer of *iqgap2*. This work underscores the fact that proteins like DiscI contribute in diverse ways to the activities necessary for optimal cell function.

Introduction

Many biological processes require cells to sense and adapt to their physical surroundings. This adaptability allows cells to perform robust cell shape changes. Processes ranging from cytokinesis and cell migration to more complex events such as development require integration of internal and external mechanical cues to exert these physical changes (Blanchoin et al., 2014; Sinha et al., 2017; Umbarger, 1956). To integrate these internal and external cues, cells leverage their contractility machinery, which includes actin filaments, Myosin II (MyoII) motors, crosslinkers, and other scaffolding proteins. These proteins compose a mechanoresponsive system that senses and then responds to chemical and mechanical signals by accumulating locally to drive and ensure high fidelity cell shape changes (Kee et al., 2012; Luo et al., 2012; Schiffhauer et al., 2017; Srivastava et al., 2016; West-Foyle and Robinson, 2012).

Within the contractile machinery, MyoII and Cortexillin I (CortI) serve as key sensors and actuators of applied mechanical stress. These proteins provide the cells with the ability to quickly respond and adapt to external mechanical stimuli. These same mechanoresponsive proteins also accumulate at the cleavage furrow cortex of a dividing cell to promote contractility. Altogether, this mechanoresponsiveness of the contractility machinery provides a quality control function that ensures that the cell completes cytokinesis with high fidelity despite mechanical disturbances (Kee et al., 2012; Liu and Robinson, 2018;

Murthy and Wadsworth, 2005; Nguyen et al., 2022; Yumura et al., 2008). Along with other actin crosslinkers, this system collectively bears the mechanical load at the cell cortex, and loss of these proteins leads to altered physical properties of cortex, resulting in changes in cell behaviors (Ren et al., 2009). Therefore, this machinery allows cells to exert robust control and modulation on multiple processes that involve cell shape modifications.

An interdependency of the cytoskeletal machinery exists within the contractile machinery. For example, mechanoreponsive proteins like MyoII and CortI cooperatively accumulate at sites of mechanical perturbations (Kee et al., 2012; Kothari et al., 2019a; Ren et al., 2009; Schiffhauer et al., 2017). In contrast, mechanisms exist to prevent overaccumulation and hyperactivity of this system. Two CortI-binding proteins, IQGAP1 and IQGAP2, provide a higher level of regulation on this mechanoresponsive system. IQGAP1 inhibits the mechanoresponsive accumulation of MyoII and CortI, while IQGAP2 relieves this repression. In the absence of IQGAP2, MyoII and CortI fail to accumulate in response to externally applied perturbations due to inhibition by IQGAP1 (Kee et al., 2012; Kothari et al., 2019b; Srivastava et al., 2016). These mechanical feedback systems spatially and temporally tune the level of MyoII and CortI accumulation and contractility.

Previously, we found that several key proteins of the mechanosensory system preassemble in the cytoplasm,

[1]Department of Cell Biology, School of Medicine, Johns Hopkins University, Baltimore, MD.

Correspondence to Douglas N. Robinson: dnr@jhmi.edu.

forming mechanoresponsive (contains IQGAP2) and non-mechanoresponsive (contains IQGAP1) complexes that we term contractility kits (CKs; Kothari et al., 2019b). While the contractility network involves a much larger cohort of proteins, the proteins in the CKs encompass a smaller subset that allows for delivery of key cytoskeletal proteins such as CortI and MyoII to the cortex (Fig. 1 A). A likely benefit of being "pre-assembled" in the cytoplasm is that it may allow the CKs to respond more rapidly to mechanical disturbances and/or stimuli. IQGAP2 and IQGAP1 are key regulators of these CKs and aid in controlling the level of the proteins that accumulate at the cortex, i.e., they likely help establish the setpoint and responsiveness of the system. The CK concept, hence, accounts for how so many proteins can be directed rapidly and synchronously in response to discrete cues, such as from mechanical stresses. In addition to the CKs, we found that the CK network includes several other proteins, including Discoidin I (DscI; Kothari et al., 2019b). In Kothari et al. (2019b), using liquid chromatography–mass spectrometry, DscI was detected as a biochemical interactor of IQGAP2 in both cytosolic and cytoskeletal fractions of FLAG–GFP–IQGAP2 in iqg2-null cells. Furthermore, using fluorescence cross-correlation spectroscopy (FCCS), a method to measure in vivo interactions, the authors detected interactions of DscI with both CortI and IQGAP2 within the cytoplasm. Interestingly, DscI also was recovered as a genetic suppressor of cortI null mutants through a suppressor screen where Dsc overexpression rescue the developmental phenotypes of cortI null cells (Nguyen and Robinson, 2020; Robinson and Spudich, 2000). These results indicate a possible role of Dsc proteins in the mechanobiome.

DscI belongs to the discoidin protein family, consisting of DscI and DscII, which are N-acetylgalactosamine-binding lectins found in Dictyostelium discoideum and expressed as Dictyostelium enters the developmental phase (Alexander et al., 1983; Frazier et al., 1975; Rosen et al., 1973). The DscI family is composed of three highly homologous dsc1 genes: dsc1A, C, and D. DscI was first suggested to play a role in mediating cell–cell and cell–substrate interactions, due to its lectin properties (Berger and Armant, 1982; Springer and Barondes, 1980; Springer et al., 1984). Structurally, DscI consists of two domains: an N-terminal discoidin domain and a C-terminal lectin domain. The N-terminal discoidin domain contains a motif that has diverse functions in mediating interactions with various molecules in both eukaryotes and prokaryotes. The C-terminal domain is an H-type lectin domain that facilitates hemaglutination activity (Baumgartner et al., 1998; Kiedzierska et al., 2007). Dsc was traditionally thought to be mainly involved in cell surface signaling and glycoconjugate binding and is required for aggregation and development since univalent anti-DscI blocked aggregation in WT cells (Springer and Barondes, 1980). Several other studies have indicated that DscI functions in the ECM and was detected in the ECM through a proteomics analysis (Huber and O'Day, 2015). While most studies have focused on DscI's extracellular functions, some studies have alluded to its possible intracellular roles. In one study, using immunofluorescence, DscI was observed to reside in the cytoplasm of vegetative Dictyostelium cells (Alexander et al., 1992). In another, DscI was located intracellularly inside vesicles of developmental cells (Barondes et al., 1985).

In this study, we find that DscI has important roles intracellularly, specifically within the CK machinery. We found that dsc1 null single mutants have a mild cytokinesis defect, reduced cortical tension, and impaired CortI mechanoresponsiveness (the ability to accumulate in response to mechanical stress). Deletion of dsc1 also acts as genetic suppressor of cortI and iqgap1 null mutants, but as a genetic enhancer of iqgap2 null mutants. Furthermore, transcript and protein expression of DscI are tightly controlled by CortI and IQGAP1. In addition, DscI localizes to the cortex and helps with CortI cortical association. This association is crucial for the integrity of the cortex and the membrane since the deletion of dsc1 results in atypical outpouching of the cell cortex and plasma membrane. We also find that absence of DscI weakens the interactions of CortI with IQGAP2 and MyoII as assessed by FCCS. These observations support the notion that these proteins function in a complex, and DscI helps stabilize the assembly of CortI into this complex. In short, DscI is necessary for full function of the CK system. Overall, this work re-emphasizes the point that many proteins contribute in multiple diverse ways to the function of the cell, and it is increasingly apparent that proteins may not be described as providing a single function for the cell.

Results

DscI is crucial for normal growth and cytokinesis

To begin deciphering the roles of DscI, we first studied the cytokinetic defects of cells lacking DscI by generating knockout (KO) mutants using CRISPR/Cas9 (Sekine et al., 2018). A gRNA sequence complementary to a gene coding sequence close to the 5′ end that is identical in all three dsc1 paralogs was designed to direct gene specificity. KO mutants were confirmed using Western (Fig. 1 B and Fig. S1 A) and sequence analysis (Fig. S1 B). Western quantification showed complete absence of DscI protein in various clones (Fig. 1 C and Fig. S1 C) in two separate D. discoideum backgrounds. Sequence analysis of the clones generated in the Ax2 background showed that most mutant clones obtain mutations at the targeted dsc1A gene (Fig. S1 B). Sequencing analysis cannot be performed in the KAx3 background due to the duplication of the dsc1 genes on chromosome 2. In the mutants analyzed, only the gene sequence of dsc1A was altered, while that of dsc1C and dsc1D remained intact (not shown). This observation indicates that mutating dsc1A gene is sufficient to obliterate DscI protein expression in vegetative cells. Quantitative RT-PCR (qRT-PCR) experiments (Fig. 6 C) also confirm that dsc1 transcripts were absent in these cells. These results suggest that dsc1C and dsc1D are not expressed in vegetative cells. Therefore, from this point on, we refer to DscIA as DscI as it is likely the only functional paralog in vegetative cells.

Cytokinesis and cell growth are required for cells to multiply and require extensive cell shape changes, and cell growth may be impaired due to defects in cytokinesis. We used suspension growth, a highly restrictive growth condition for impaired cytokinesis (Adachi, 2001; Uyeda et al., 2000), to assess whether DscI is essential for cell growth and for cytokinesis. We found
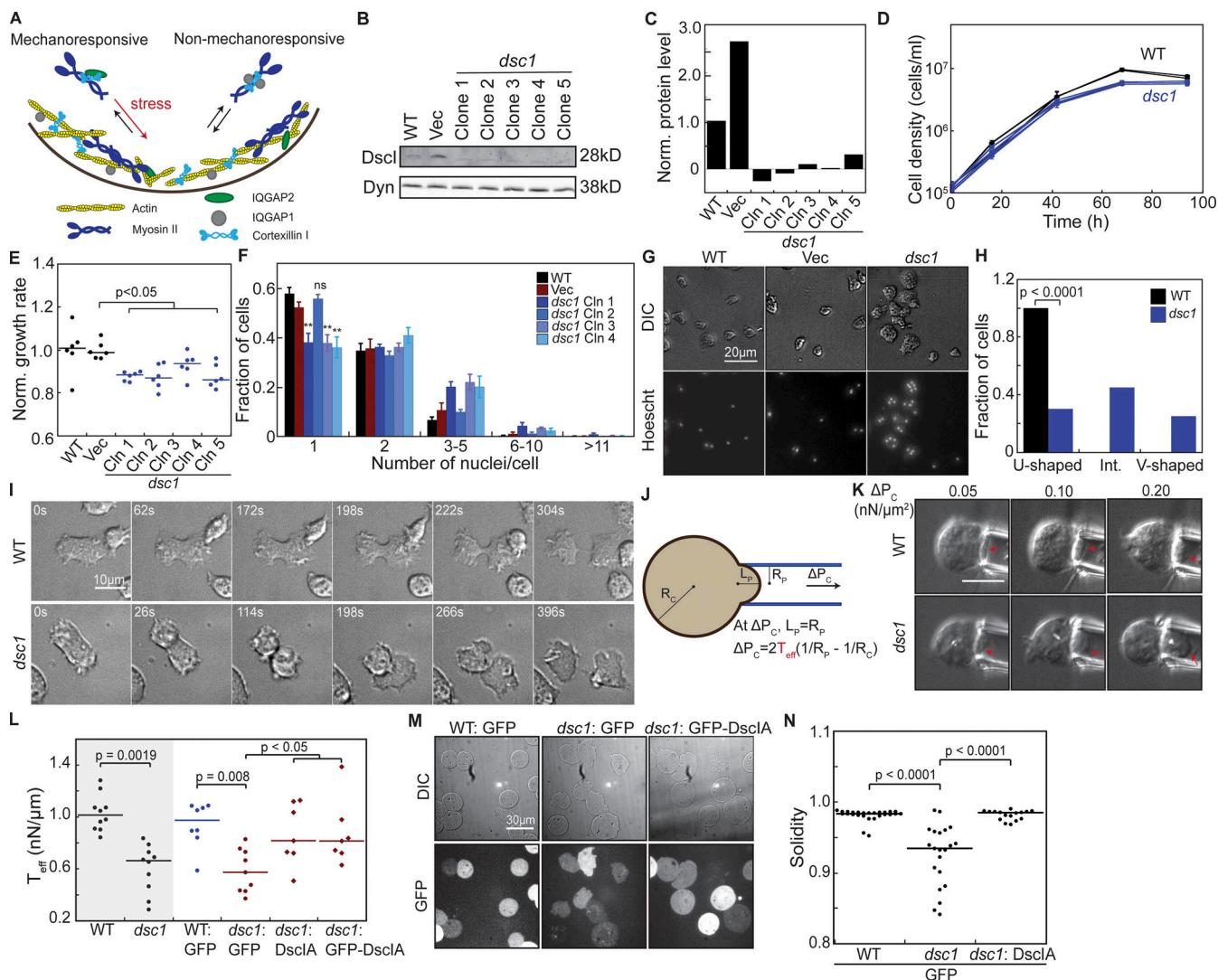
Figure 1. DscI is required for normal growth, cytokinesis, and cortical integrity. (A) The CKs pre-assemble in the cytoplasm and accumulate quickly to the cortex upon mechanical stimuli. **(B and C)** *dsc1* null mutant clones generated in the KAx3 background were verified using Western analysis. Western blot showed deletion of DscI bands, quantified and normalized to WT level in C, in all *dsc1* null mutant clones. Dynacortin (Dyn) is provided as a loading control. **(D)** Representative growth curves show that *dsc1* null mutants have mild growth defects in suspension culture. Cell densities, as indicated, are plotted as a function of time. Growth curves for control cell lines are shown in black and those for *dsc1* null mutant clones are shown in blue. Number of samples = 3 per growth curve; bars represent the SEM. Some SEM bars are smaller than the symbols. **(E)** Growth rates quantified during exponential growth and normalized to WT reveal significant reduction in suspension culture growth in different *dsc1* mutant clones. Growth rate of each cell line was normalized to that of WT control. Number of samples analyzed, *n* = 6 from two independent experiments. **(F)** Quantification of the number of nuclei per cell when cells were 3 d in suspension culture. All but one of *dsc1* mutants became more multinucleated, especially within 3–5 nuclei/cell. *n* = 4 per cell line, with 100–200 cells per cell line quantified per replicate. P values were calculated using the ANOVA followed by Fisher's LSD test based on the single nuclei/cell fraction subset (**, P < 0.001). **(G)** Images of DIC channel and nuclear staining by Hoescht reveal a slight increase in cell size as well as number of nuclei in each cell in several *dsc1* clones. DIC and Hoescht images for WT are reproduced in Fig. 4 C. **(H)** Graph shows fraction of WT and *dsc1* cells having a WT-like U-shaped cleavage furrow, an aberrant V-shaped furrow, or an intermediate furrow during cytokinesis. An intermediate furrow is one that shows both a U-shaped and V-shaped furrow along different stages of cytokinesis. *n* = 28 for WT and *n* = 20 for *dsc1*. P value was calculated using the Comparison of Proportions test. **(I)** Images of different stages of cytokinesis of a WT cell and a *dsc1* cell having a V-shaped furrow. Images were collected from cells at 70% confluency, and *t* = 0 is defined as the time when each video begins. Full video of WT and *dsc1* dividing cells are provided in the Supplemental materials (Videos 1 and 2). **(J)** The diagram shows the manipulation of cells by MPA for cortical tension and mechanoresponsiveness analysis. For cortical tension measurements, the pressure is increased until the length (L_p) of the region of the cell pulled into the micropipette equals the radius of the pipette (R_p). At this equilibrium pressure (ΔP_c), the radius of the cell at can be quantified, and the effective cortical tension T_{eff} is calculated from the equation shown in the panel. **(K)** *dsc1* mutant cells have a higher degree of deformation when aspirated at the same negative pressure compared to WT cells. Red arrows show the front of the cell inside the micropipette. Scale bar, 10 μm and applies to all panels. **(L)** The effective cortical tension values of WT, *dsc1*, and *dsc1*-complemented cells were quantified as detailed in the Materials and methods. Gray background indicates non-transformed cell lines. P values were calculated using Kruskal-Wallis followed by Wilcoxon test. Number of cells measured, *n* = 7–10 from three independent experiments. **(M)** When compressed using agarose overlay, which introduces mechanical stress to the cortex, *dsc1* mutant cells expressing only GFP displayed a bleb-like morphology. This morphology was observed in both DIC and GFP channels. This phenotype was rescued to WT levels in *dsc1*:: GFP-DscIA cells. **(N)** *dsc1* mutants displayed a significant reduction in solidity, a measure of smoothness of the cell periphery, when subjected to mechanical stress, as compared to WT control and rescue control (Kruskal-Wallis, P < 0.0001; Wilcoxon, P < 0.0001). Number of cells analyzed, *n* = 17–28 from two independent experiments. Solidity measurement was analyzed using ImageJ and calculated as the area of a particle divided by its convex hull area. Source data are available for this figure: SourceData F1.

that *dsc1* mutants grow slightly more slowly (Fig. 1 D and Fig. S1 D), yielding a mild, yet significant, growth rate reduction (Fig. 1 E, and Fig. S1 E) as compared to WT controls. These mutants also saturate at a lower cell density than WT parental cells (Fig. S1 F).

Another prominent defect of cytokinesis is the presence of multinucleated cells, especially when grown in suspension culture (Park et al., 2018; Rivero et al., 2002). When cells cannot complete cytokinesis successfully, these uncompleted events lead to the accumulation of multiple nuclei within a cell. Within 3 d in suspension, with the exception of one clone, cells lacking DscI accumulated more nuclei within the cytoplasm, largely in the range of 3–5 nuclei/cell (Fig. 1, F and G; and Fig. S1 G). As a result, *dsc1* null cells generally appear bigger than WT cells due to the increase in multinucleation (Fig. 1 G). Defects in both growth and multinucleation were observed across multiple mutant clones in two different strain backgrounds. Among more than seven mutants tested, only one mutant did not display increased multinucleation. This difference is likely due to clonal variation as these mutants were subcloned from the parental cell line during the process of mutant generation. *dsc1* mutant clone 4 was randomly selected for subsequent experiments. Importantly, when the *dsc1* mutant was complemented with DscIA, both growth and multinucleation defects were rescued, confirming that these defects are attributed to the absence of DscIA (Fig. S2, A–D).

A majority of *dsc1* cells displayed aberrant morphology during different stages of cytokinesis when grown on surfaces. Normally, WT *Dictostelium* cells undergo a characteristic sequence of steps that include cleavage furrow formation, ingression, and abcission during cytokinesis. A WT cleavage furrow displays a characteristic U shape (Fig. 1, H and I; Videos 1 and 2) that gradually ingresses to form a thin bridge, which is then severed. In *dsc1* cells, only 30% of the cells maintain WT-like furrow morphology. 30% of *dsc1* cells have abnormally shaped furrows, which is more V-shaped and less visible throughout cytokinesis (Fig. 1, H and I; Videos 1 and 2). The rest of *dsc1* cells display a mix of U-shaped and V-shaped morphologies, described as an "intermediate furrrow morphology." Since DscI is implicated in cell-substrate adhesion, this abnormal V-shaped morphology may be due to defects in adhesion as *dsc1* cells divide. This adhesion defect, however, was not observed across the whole population of cells, which is primarily composed of interphase cells (Fig. S1 G). Hence, it is likely that in vegetative cells, *dsc1* is important for adhesion primarily during cytokinesis. Altogether, these observations reveal an important role of DscI in ensuring cytokinesis fidelity.

A crucial role of the contractile machinery is to provide the cortical mechanical properties, which are largely defined by the actin cytoskeleton (Efremov et al., 2015; Fritzsche et al., 2016; Luo and Robinson, 2011; Ren et al., 2009). Since DscI interacts with several members of the contractile machinery, to test if DscI impacts cortical mechanics, we used micropipette aspiration (MPA) to measure the degree of deformability in *dsc1* null cells (Fig. 1 J). The *dsc1* null cells were more deformable when aspiration pressure was applied to the cortex (Fig. 1 K). In the example shown (Fig. 1 K), the WT cell required 0.20 nN/µm² pressure to reach the critical pressure at which the length of the

cell inside the pipette (L_p) is equal to the pipette radius (R_c). In contrast, the *dsc1* mutant cell only required 0.05 nN/µm² of pressure to deform to the same extent. The average effective cortical tension, a measure of deformability, of *dsc1* cells is 0.66 nN/µm, which is significantly lower than that of WT cells (1.0 nN/µm; Fig. 1 L). Furthermore, when these cells are mechanically challenged using agarose overlay, *dsc1* null cells displayed aberrant membrane morphology, characterized by significant cortical out-pouching, i.e., bleb-like structures (Fig. 1 M). The degree of bleb-like formation is quantified as changes in solidity of the cell membrane (Fig. 1 N). The bleb-like structures on the mechanically challenged membrane usually indicate accumulated tension at the cortex due to increase MyoII activity and/or weakened linkages between the cortex and membrane (Charras et al., 2006; Chikina et al., 2019; Ghosh et al., 2021; Luo et al., 2012). These defects in cortical functions were rescued in *dsc1* null-complemented cells (Fig. 1, L–N), indicating that they are specifically attributed to the absence of DscI. Altogether, these results indicate another function of DscI is to ensure cortical mechanical integrity.

Balanced expression of dscI directs cortI cortical distribution

DscI has cytoplasmic and membrane-associated distributions in developing cells (Alexander et al., 1992; Barondes et al., 1985; Fukuzawa and Ochiai, 1993). Given the cortical phenotypes, including reduced cortical tension, we examined the subcellular distribution of DscI in vegetative WT cells. Using immunofluorescence imaging, we found that the majority of DscI stays in the cytoplasm while a portion of the protein enriches at the cell cortex (Fig. 2 A). This observation is consistent with the fact that many DscI interactors also localize to the cortex, notably IQGAP2 and CortI (Kothari et al., 2019b). However, unlike CortI, which localizes to the cleavage furrow cortex, immunofluorescence imaging in fixed and live cells showed that DscIA does not concentrate at the cleavage furrow as vegetative cells undergo cytokinesis (Fig. 2, B and C; Video 3; and Fig. S4, A and B; Kee et al., 2012; Liu and Robinson, 2018; Murthy and Wadsworth, 2005; Yumura et al., 2008).

Previous studies established that CortI, in particular, serves as a cortical actin crosslinker and actin-membrane tether, and *cortI* null mutants have similar aberrant cell behaviors and cortical mechanics as observed for *dsc1* (Kee et al., 2012; Simson et al., 1998; Stock et al., 1999; Weber et al., 1999). DscI may then help CortI carry out its cortical functions. Indeed, we observed that in *dsc1* nulls, the cortical localization of CortI is severely disrupted (Fig. 2, D and G; and Fig. S2, E and F). Since DscI also interacts with other cytoskeletal proteins such as IQGAP2 (Kothari et al., 2019b), we investigated whether localization of IQGAP2 and MyoII is impacted in *dsc1* null cells. However, the cortical localization of these proteins was unchanged in *dsc1* null cells (Fig. S3, A–D). We then asked if overexpression of DscIA would affect the distribution of CortI. We found that when DscI is overexpressed, CortI cortical distribution is also significantly disrupted (Fig. 2, E–G).

These collective observations indicate that DscI levels reside near an optimal sweetspot, not too little or not too much, in WT cells to ensure a normal CortI accumulation at the cortex (Fig. 2 H).
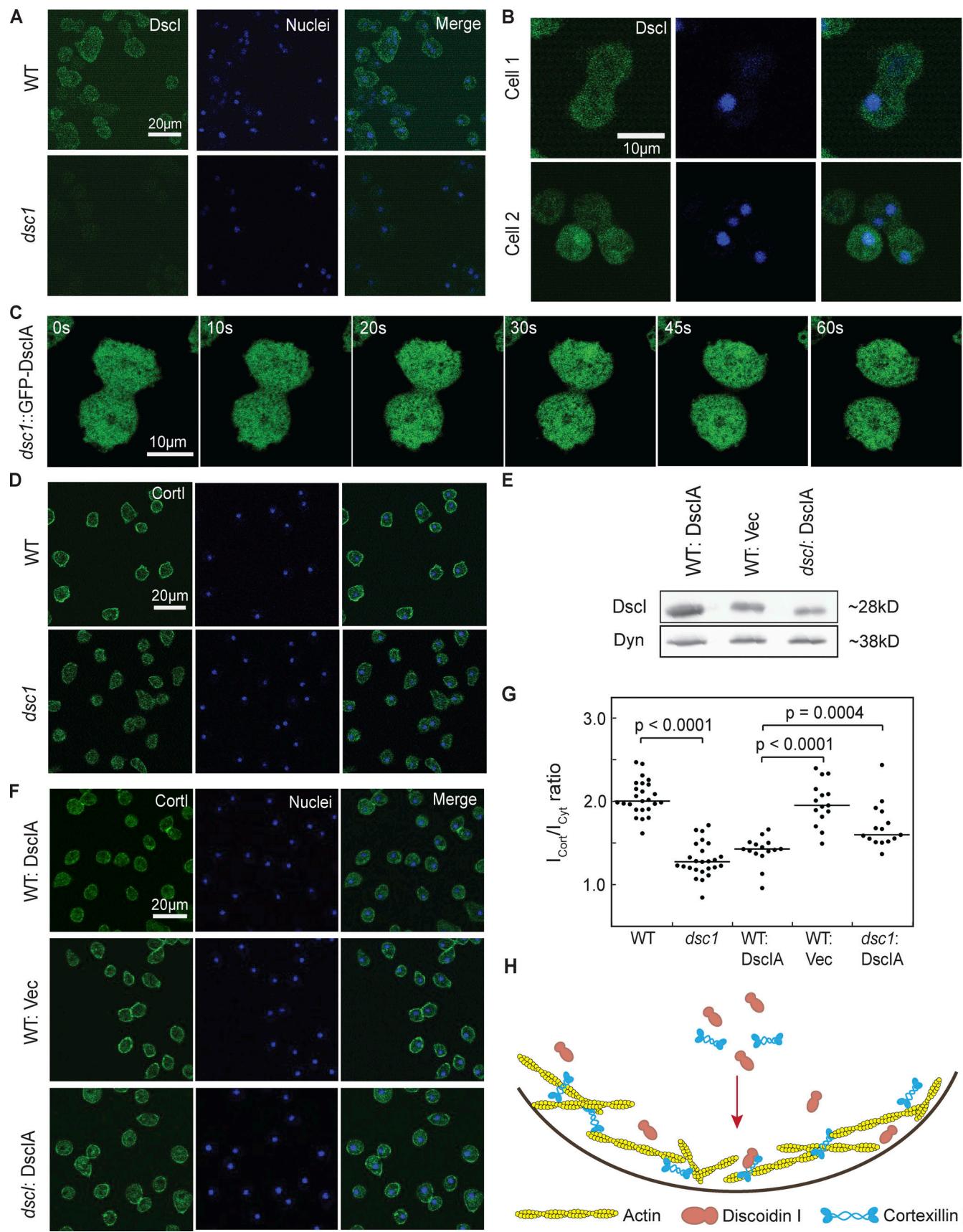
Figure 2. **A portion of DscI localizes to the cortex, and Dsc is needed for CortI cortical distribution. (A)** Representative images of immunofluorescence imaging of DscI (green) using anti-DscI antibody and nuclei (blue) labeled with Hoescht in WT and *dsc1* cells. Images were collected using confocal microscopy.

DscI signal was present in the cytoplasm and slightly enriched in the cortex of WT cells. This signal was absent in *dsc1* null cells, confirming the antibody's specificity for DscI. **(B)** Representative images of immunofluorescence imaging of DscI (green) using anti-DscI antibody and nuclei (blue) labeled with Hoescht in dividing WT cells. **(C)** Time series of a *dsc1* null-complemented cell completing cytokinesis. DscIA was fused with GFP and images were collected with a GFP channel on an Olympus IX71 microscope, equipped with a 40× (NA 1.30) oil objective at room temperature using Zen software and analyzed with ImageJ. $t = 0$ is defined as the time when the video began. The video is provided in the Supplemental materials (Video 3). **(D and F)** Representative confocal immunofluorescence images of WT, *dsc1* null, DscIA-overexpressed, vector control (Vec) and *dsc1* null-complemented cells stained with anti-CortI (green) and Hoescht to label nuclei (blue). Images were collected using a Zeiss AxioObserver with 780-Quasar confocal module microscope, equipped with a C-Apochromat 40× (NA 1.2) water objective at room temperature using Zen software and analyzed with ImageJ. Vector encoding mCherry was used as the vector (Vec) control. **(E)** Western blot verifying overexpression of DscIA in WT background cells is shown. Dynacortin (Dyn) is provided as a loading control. **(G)** CortI cortical localization for D and F was quantified as the ratio of mean signal intensity at the cortex (I_{cort}) to the mean signal intensity of the cytoplasm (I_{cyt}). P values were calculated using the ANOVA followed by Fisher's LSD test. Number of cells analyzed, $n = 15$–25 from two independent experiments. **(H)** Summary diagram shows that a fraction of intracellular DscI localizes to the cortex, and DscI helps with cortical distribution of CortI. Source data are available for this figure: SourceData F2.

CortI requires dscI to mechanorespond and accumulate at the cleavage furrow cortex

Many proteins within the CK network such as MyoII, CortI, and IQGAP2 can mechanorespond, which is defined as the ability of the protein to accumulate locally in response to applied mechanical stress (Effler et al., 2006; Kee et al., 2012; Ren et al., 2009). Since DscI helps maintain cortical integrity and is partially localized at the cortex, this raised the question whether DscI itself can mechanorespond. Therefore, we used MPA to aspirate *dsc1* mutant cells expressing GFP-DscIA and examined if GFP-DscIA accumulates at the site of aspiration. No GFP-DscIA was detected at the cortex inside the pipette (Fig. 3 A). The quantified ratio of cortical GFP signal intensity inside the pipette to the opposite cortex (I_p/I_o) is not different than that of the GFP control and is significantly lower than that of GFP-MyoII, a positive control (Fig. 3 D).

We then tested if DscIA is required for other mechanoresponsive proteins to accumulate at sites of mechanical stress. We used MPA to apply stress to GFP-CortI expressing *cortI* single and *cortI; dsc1* double mutants. GFP-CortI failed to accumulate at the cortex inside the pipette when *dsc1* was deleted (Fig. 3 B). This reduction in CortI's mechanoresponsiveness is reflected in the significant difference in the I_p/I_o values between GFP-CortI signal in *cortI* and *cortI; dsc1* background (Fig. 3 D). In fact, the level of GFP-CortI accumulation at the aspirated cortex in the double mutant is similar to that of the GFP-alone control. Furthermore, CortI accumulation at the cleavage furrow cortex is also significantly reduced when DscIA is absent (Fig. S4, D and E). In contrast, *dsc1* deletion does not inhibit GFP-MyoII's mechanoresponsiveness or ability to localize to the cleavage furrow cortex (Fig. 3, C and D; and Fig. S4, C and E). Interestingly, overexpression of DscI does not inhibit CortI's mechanoresponsiveness, although it does significantly reduce cortical CortI (Fig. S4, F and G). This observation suggests that once a certain threshold of CortI's ability to associate with the cortex is reached, CortI can mechanorespond.

Altogether, DscIA does not accumulate locally in response to mechanical stress, but its presence is crucial for CortI's, but not MyoII's, mechanoresponsiveness.

DscI is antagonized by non-mechanoresponsive CK components

Previous genetic dissection demonstrated that IQGAP proteins, including IQGAP1 and IQGAP2, modulate the activity and mechanoresponsivenes of MyoII and CortI (Kee et al., 2012; Srivastava and Robinson, 2015). IQGAP1 is a negative regulator as it inhibits the mechanoresponsive accumulation of CortI and MyoII. IQGAP2, in contrast, relieves this repression, allowing the proteins to accumulate in response to mechanical stress (Kee et al., 2012; Kothari et al., 2019a; Ren et al., 2014; Srivastava and Robinson, 2015). These IQGAP proteins pre-assemble into antagonistic CKs with MyoII and CortI in the cytoplasm and actively fine-tune the level of the contractile system at the cortex (Kothari et al., 2019b). Therefore, we asked if DscI functions in the same regulatory pathway, and potentially the same CK complexes. To address this question, we used CRISPR/Cas9 to generate double mutants that lack *dsc1* and *cortI*, *iqgap1*, or *iqgap2* and examined their genetic interactions using suspension growth. We first examined the genetic relationship between *dsc1* and *cortI*. We grew WT, *dsc1* and *cortI* single-mutant, and *cortI; dsc1* double-mutant cells in suspension and analyzed their growth rates. Strikingly, deleting *dsc1* in *cortI* null cells significantly improved their growth, compared to *cortI* single mutants (Fig. 4 A). The average growth rate of *cortI; dsc1* cells ($k = 0.052$ h^{-1}) was significantly faster than the *cortI* cells ($k = 0.027$ h^{-1}) and similar to the growth rate measured for the *dsc1* cells ($k = 0.053$ h^{-1}; Fig. 4 B). Consistent with the improved growth rate, *cortI; dsc1* double-mutant cells were also less multinucleated when compared to *cortI* single-mutant cells (Fig. 4 C). Compared to the WT, *cortI* single-mutant cells are severely multinucleated with the majority of cells enlarged, having more than five nuclei. However, the *cortI; dsc1* double-mutant cells had lower multinucleation and normal cell size (Fig. 4, C and D). These observations indicate an antagonistic relationship between DscI and CortI.

We next tested how DscI interacts with IQGAP1. We knocked *dscIA* out of the *iqgap1* null cells and found that DscI and IQGAP1 also work antagonistically. Suspension growth curves reveal that *iqgap1; dsc1* cells ($k = 0.04$ h^{-1}) grow faster than *iqgap1* single-mutant cells ($k = 0.027$ h^{-1}), although these double-mutant cells still grow slightly slower than *dsc1* single-mutant cells ($k = 0.049$ h^{-1}; Fig. 4, E and F). Interestingly, these interactions are very similar to those observed between DscI and CortI. The magnitudes of changes in growth and multinucleation are comparable between the two double mutants (*cortI; dsc1* and *iqgap1; dsc1*) and were rescuable back to the single-mutant rates (Fig. S5, A and B). Overall, DscI activity is inhibited by IQGAP1 and CortI.
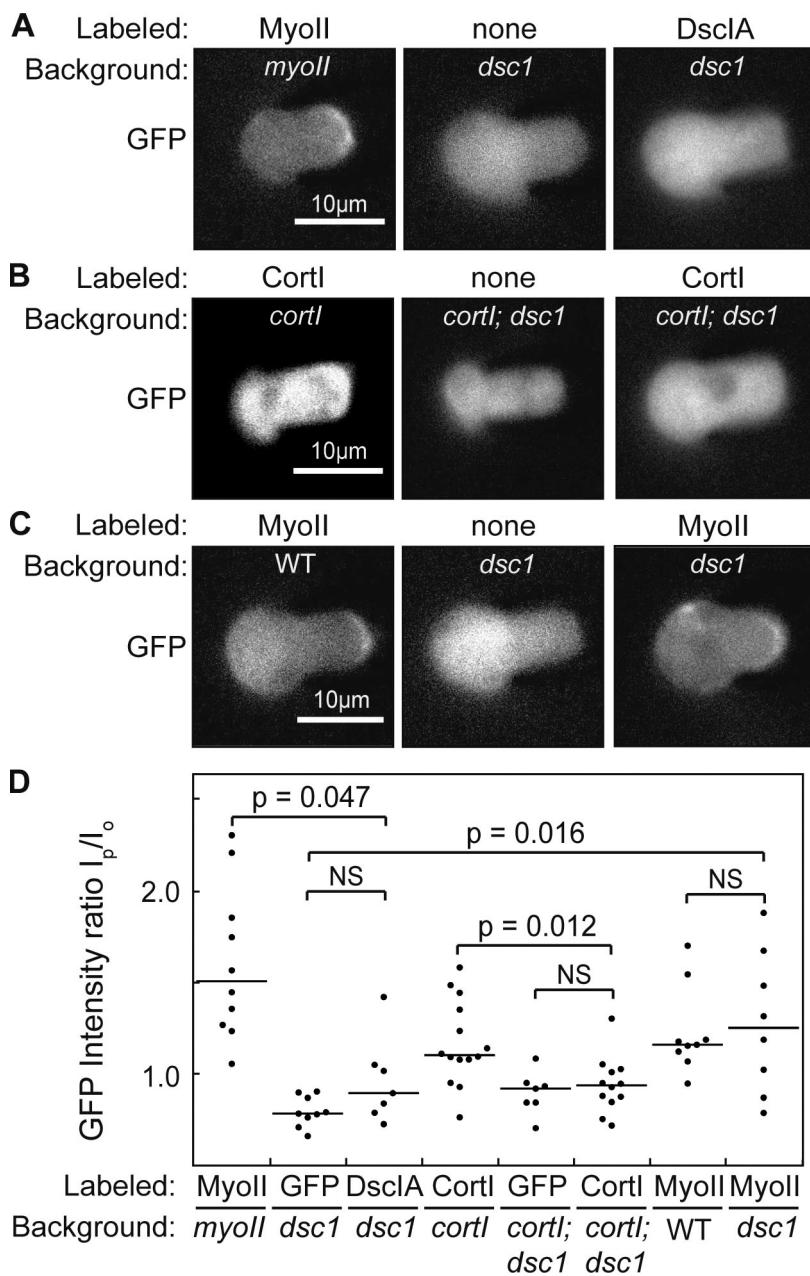
Figure 3. **DscI facilitates the mechanoresponsiveness of CortI. (A)** GFP images show localization of GFP-MyoII, GFP-alone, and GFP-DscIA as cells are aspirated with a micropipette (from left to right). GFP-MyoII serves as a positive control. **(B)** GFP images show localization of GFP-CortI in cells with and without DscI as these cells are aspirated with a micropipette. **(C)** GFP images show localization of GFP-MyoII in cells with and without DscI as these cells are aspirated with a micropipette. GFP-alone serves as a negative control. For A–C, the genetic background of each cell line is indicated in the upper edge of each image, and GFP-alone serves as a negative control. Micropipette suction pressure was applied to the right side of each cell. **(D)** The degree of mechanoresponsiveness of GFP-tagged proteins is quantified as the GFP intensity ratio (I_p/I_o) of the cortex inside the pipette (I_p) to the cortex on the opposite side of the cell (I_o). P values were derived from Kruskal Wallis followed by the Wilcoxon test. In A–D, "labeled" indicates the protein labeled by GFP, and "background" indicates the genetic background (WT or specific single or double null) expressing the labeled protein. Number of cells analyzed, n = 7–10 from four independent experiments.

Given the genetic interactions between DscI and IQGAP1 along with genetic and biochemical interactions between CortI and DscI, we next tested if DscI and IQGAP1 interact in the cytoplasm. We used FCCS in live interphase cells. This technique allows us to quantitatively characterize protein–protein interactions in a defined confocal volume within the cytoplasm (Bacia et al., 2006; Kothari et al., 2019b). The interaction of separately expressed GFP and mCherry acts as a negative control with a median apparent K_D of 5.0 μM while that of fusion GFP-mCherry acts as a positive control with a median K_D of 1.1 μM. The apparent K_D measured by FCCS between DscI and IQGAP1 in both WT and complemented-null backgrounds are similar to each other and the negative control, suggesting that IQGAP1 and DscI do not appreciably biochemically interact in vivo (Fig. S5 C). Both IQGAPs are a conserved family of proteins characterized by a GAP-like domain that can bind Rac family small GTPases. Structurally, mammalian IQGAP proteins have an N-terminal calponin homology (CH) motif, which functions as an F-actin binding domain (Brill et al., 1996; Hart et al., 1996). In addition, the mammalian IQGAPs have multiple isoleucine-glutamine (IQ) (calponin-binding) domains and a tryptophan-tryptophan (WW) protein-interaction motif. However, in *Dictyostelium*, neither IQGAP1 nor IQGAP2 contain the CH, WW, or IQ domains (Adachi et al., 1997). Both IQGAP1 and IQGAP2 are present in the cytoplasm and accumulate at the cortex, and during cytokinesis, they enrich at the cleavage furrow cortex (Faix et al., 2001; Mondal et al., 2010). In terms of sequence, they are 52% identical and 70% similar in amino acid sequence, accounting for why DscI interacts with IQGAP2, but not IQGAP1.
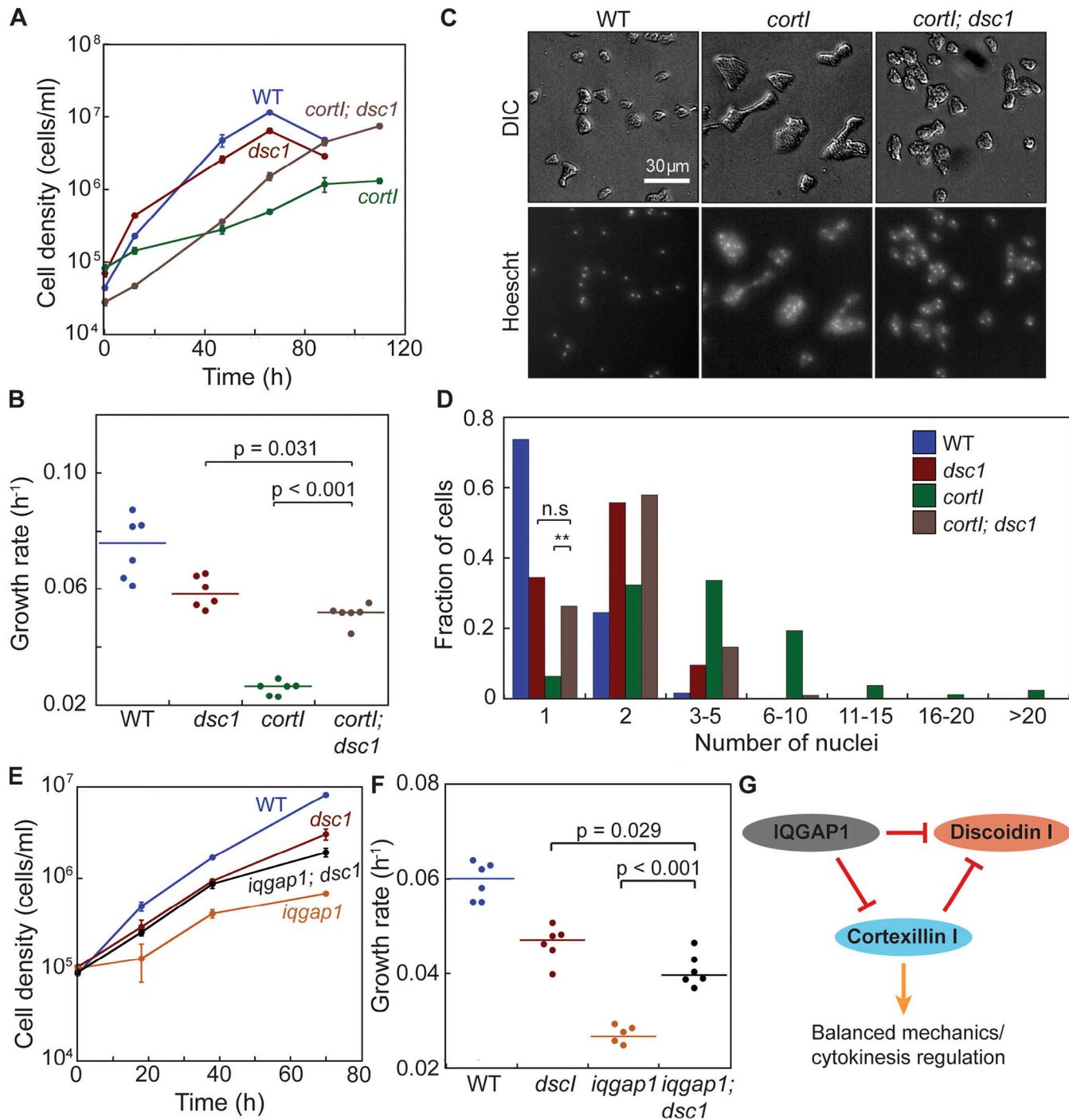
Figure 4. **DscI is antagonized by CortI and IQGAP1, which serves as a negative regulator of CK mechanoresponsiveness. (A)** Representative growth curves in suspension culture of WT (blue), *dsc1* (red), and *cortI* (green) single mutants and *cortI; dsc1* (brown) double mutant. Growth curve of *cortI; dsc1* shows faster growth, as compared to the *cortI* single mutant. *n* = 3 per growth curve; bars represent SEM. **(B)** The quantified growth rates for the exponential growth phase for each cell line shown in A are presented. The average growth rate of *cortI; dsc1* (0.051 h⁻¹) was significantly higher than that of *cortI* (0.026 h⁻¹) and was lower than *dsc1* single mutants (0.059 h⁻¹). P values were calculated using ANOVA followed by Fisher's LSD test. Number of samples analyzed, *n* = 6 from two independent experiments. **(C)** Representative images of DIC and nuclei show relative cell size and number of nuclei/cell between different cell lines. *cortI* single mutant displayed an enlarged cell size due to a higher degree of multinucleation. Cells were less multinucleated in the *cortI; dsc1* double mutant strain. DIC and Hoescht images for WT are reproduced from Fig. 1 G. **(D)** Quantification of the number of nuclei/cell for WT, *dsc1*, *cortI*, and *cortI;dsc1* after 2 d in suspension. The *cortI* mutant displayed a high number of multinucleated cells, especially in the 3–10 nuclei/cell range. Note that among these cell lines, only *cortI* accumulated >10 nuclei. The *cortI; dsc1* double mutant was less multinucleated as compared to the *cortI* single mutant, with most cells having 1–2 nuclei/ cell, similar to *dsc1* single mutant cells. The data provided represent two replicates, with 90–115 cells per cell line for each replicate. P value was calculated using the Comparison of Proportions test. (**, P < 0.001; n.s, not significant). **(E)** Representative growth curves in suspension culture of WT (blue), *dsc1* (red), and *iqgap1* (orange) single mutant cells and the *iqgap1; dsc1* double (black) mutant cells. Growth in suspension of *iqgap1; dsc1* was faster than that of *iqgap1* and slower than that of *dsc1* single mutant cells. *n* = 6 per growth curve, bars represent SEM. **(F)** Growth rates of the exponential growth phase for each cell line.

Nguyen and Robinson
Discoidin I helps assemble contractile machinery

The average growth rate of *iqgap1; dsc1* (0.041 h⁻¹) was higher than that of *iqgap1* (0.026 hr⁻¹) and lower than *dsc1* (0.048 h⁻¹). P values were derived using ANOVA followed by Fisher's LSD test. Number of samples analyzed, n = 6 from two independent experiments. **(G)** Summary diagram shows the genetic relationship between DscI, CortI, and IQGAP1. While IQGAP1 is a known inhibitor of CortI, it also antagonizes DscI. On the other hand, DscI is also antagonized by CortI, whose roles are important for balanced cellular mechanics and cytokinesis regulation.

Together, these observations indicate that DscI regulates the localization and function of CortI, but DscI itself is antagonistically regulated by components of the CKs, including CortI and IQGAP1 (Fig. 4 G). Furthermore, the FCCS results indicate that this regulation does not require IQGAP1 and DscI to interact biochemically directly or indirectly.

IQGAP2 acts synergistically with dscI

DscI was initially implicated in the CKs by the discovery of it serving as a molecular interactor of IQGAP2, the alleviator of IQGAP1's inhibition of CortI's and MyoII's mechanoresponsiveness (Kee et al., 2012; Kothari et al., 2019a; Kothari et al., 2019b; Ren et al., 2014). Therefore, we tested if and how DscI and IQGAP2 interact. We generated *iqgap2; dsc1* double-mutant cells and analyzed their phenotype. Using the suspension growth assay, we found that the *iqgap2; dsc1* double-mutant cells have the most severe growth defects, having the lowest growth rates (k = 0.018 h⁻¹) among the cell lines tested (Fig. 5, A and B). Further, the double mutants were fully rescuable to single-mutant phenotypes (Fig. S5 D). Furthermore, these cells have a high rate of multinucleation. Differential interference contrast (DIC)– and nuclei-stained images comparing *iqgap2; dsc1* to WT and *iqgap2* single-mutant cells reveal that *iqgap2; dsc1* cells are larger and more multinucleated (Fig. 5 C). While nearly 40% of *dsc1* and 50% of *iqgap2* single mutants were multinucleated, more than 70% of *iqgap2; dsc1* cells were multinucleated (Fig. 5 D). We observed many examples of *iqgap2; dsc1* cells with more than 40 nuclei (Fig. 5 C). This extreme level of multinucleation was not observed in any other single or double mutants analyzed in this study. In addition, movies of *iqgap2; dsc1* cells undergoing cytokinesis show that these cells display cleavage furrow morphology characteristic of traction-mediated cytofission (Fig. 5 E, and Videos 4 and 5). The cleavage furrow formed in this process is more elongated and highly similar to furrows formed by *myoII* null cells as they undergo traction-mediated cytofission (Neujahr et al., 1997). Traction-mediated cytofission is less efficient than mitosis-coupled cytokinesis and explains why *iqgap2; dsc1* cells are oversized and multinucleated, as observed in Fig. 5 C. We then tested if the double mutants impact cortical tension. The *iqgap2; dsc1* double-mutant cells had a significant reduction in cortical tension as compared to wild type (28% of WT) and the single mutants (Fig. 5 F). Note that the measured effective cortical tension of *iqgap2* cells is very similar to that of published data (Kee et al., 2012). Overall, the *iqgap2; dsc1* double mutant has more severe cytokinetic and mechanical phenotypes.

Overall, IQGAP2 and DscI have synergistic genetic interactions where deletion of one enhances the deletion of the other. This interaction indicates that both IQGAP2 and DscI are required for normal cytokinesis and that they work in parallel and/or collaboratively to ensure cytokinesis fidelity. This finding is particularly interesting since previous reports established that IQGAP2 is required for CortI to properly accumulate at the cleavage furrow cortex of dividing cells (Faix et al., 2001). Collectively, based on these genetic interactions, protein distributions, and the in vivo protein interactions measured in our prior FCCS studies (Kothari et al., 2019b), IQGAP2 and DscI collaborate and function together in the same complexes to ensure proper cortical localization of CortI (Fig. 5 G).

DscI expression is downregulated in the absence of the non-mechanoresponsive CK components

DscI's genetic interactions establish that DscI is negatively regulated by CortI and IQGAP1. One possible mode of regulation is through modification of transcription and protein expression. Previous studies have established the relationship between protein expression and function for cytoskeletal proteins. For instance, mammalian α-actinin regulates non-muscle myoIIB expression (Barai et al., 2021). Imbalanced expression of different MyoII isoforms also leads to changes in cell mechanics, including tension and elasticity during cell morphodynamics (Weißenbruch et al., 2021). Since well-regulated expression of DscI is important for cell function, we tested whether DscI expression is affected by deletion of any of these CK interactors. We used Western analysis to assess protein levels of DscI in *iqgap1*, *cortI*, and *iqgap2* single KO cells. Since protein level of DscI is density-dependent (Clarke et al., 1987; Jain et al., 1992; Wetterauer et al., 1995), Western analysis was performed on cells seeded at equally low and high densities. Lysates of cells seeded for 8 h were analyzed by Western blot with anti-DscI antibodies. At both densities, the levels of DscI protein are significantly lower in *iqgap1* and *cortI* cells. In *iqgap2* mutants, DscI levels were reduced at the lower density of cells (Fig. 6 A). Quantification reveals that *iqgap1* and *cortI* cells express DscI at 30 and 17% of WT levels at high density. At low density, the values for *iqgap1*, *cortI*, and *iqgap2* mutants are 30, 10, and 55% of WT control, respectively (Fig. 6 B). The low levels of DscI protein expression could be explained by either reduced transcription, translation, or decreased protein stability. To address these possibilities, *dsc1* transcript levels in these mutants were assessed. RNA from cells at an equal high density was extracted and analyzed using qRT-PCR with primers targeting all paralogs of DscI. The *dsc1* RNA levels align tightly with protein levels. Among the mutants tested, *cortI* cells had the lowest level of *dsc1* transcript, followed by *iqgap1* cells. The *iqgap2* null cells had unchanged levels of *dsc1* transcript compared to WT control (Fig. 6 C). These observations indicate that DscI protein expression is regulated, in part, at the level of transcription and/or mRNA stability. These results suggest that CortI and IQGAP1, components of the non-mechanoresponsive CKs, also negatively regulate DscI through mechanisms that alter mRNA and protein levels.
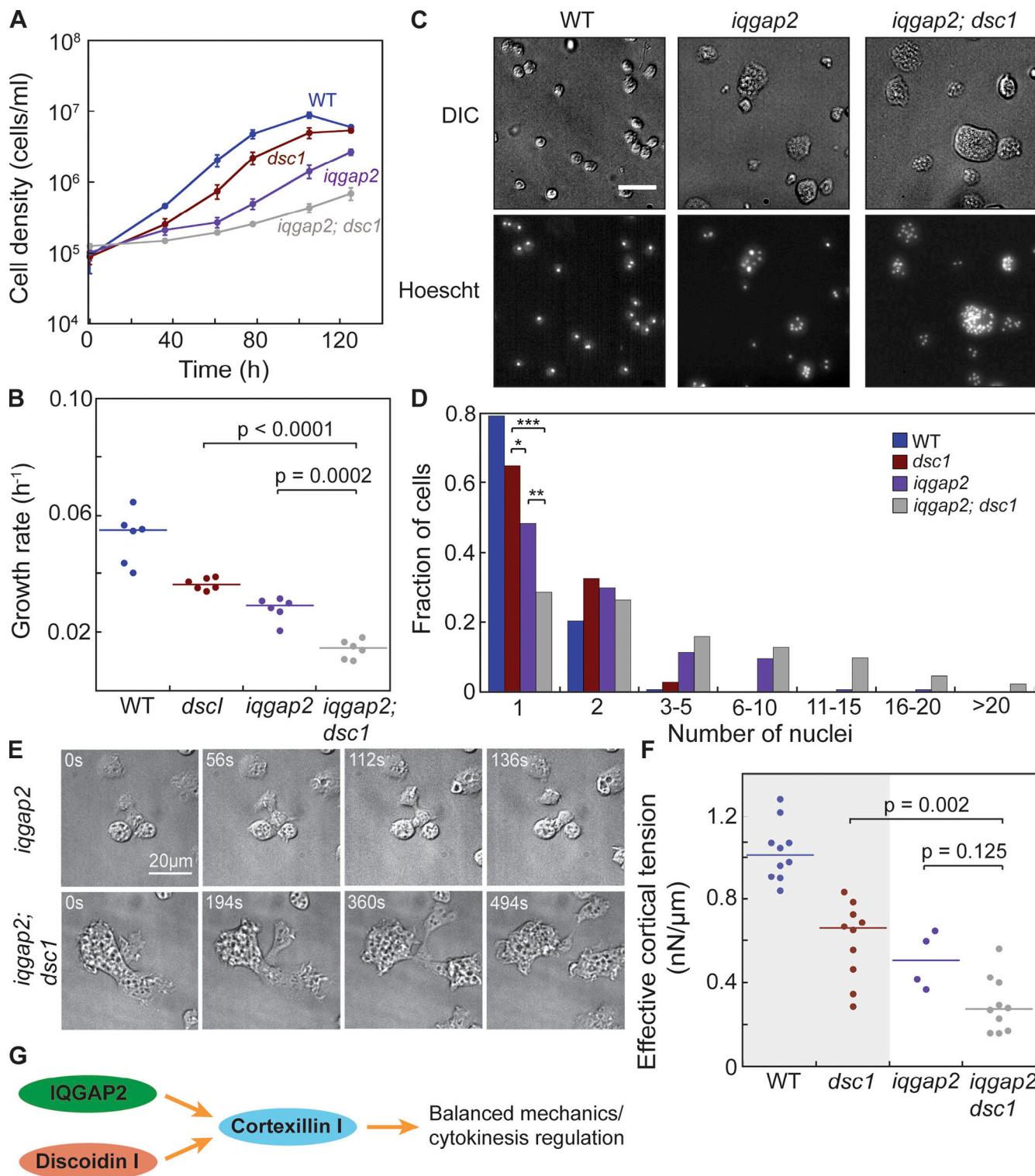
Figure 5. **Deletion of *dsc1* acts as an enhancer of *iqgap2*, which encodes a positive regulator of CK mechanoresponsiveness. (A)** Representative growth curves from suspension culture of WT (blue), *dsc1* (red), and *iqgap2* (purple) single mutants and the *iqgap2; dsc1* (gray) double mutant. Among these, *iqgap2; dsc1* had the poorest growth, followed by *iqgap2* and *dsc1* single mutants and then WT. $n = 6$ per growth curve, bars represent SEM. **(B)** Growth rates quantified from the exponential growth phase had significant differences between these cell lines. P values were derived for ANOVA followed by Fisher's LSD test. Number of samples analyzed, $n = 6$ from two independent experiments. **(C)** Representative images of DIC and nuclei stained by Hoescht of WT, *iqgap2* and *iqgap2; dsc1* mutant cell lines. Both *iqgap2* and *iqgap2; dsc1* had increased cell size and number of nuclei per cell as compared to WT. Scale bar, 40 μm and applies to all panels. **(D)** Quantification of the number of nuclei/cell revealed that *iqgap2; dsc1* cells had the greatest amount of multinucleation. Note that this double mutant strain accumulated more than 20 nuclei in cells, a level not observed in any of the single mutants. The data shown represent two replicates, with 133–182 cells per cell line for each replicate. P value was calculated using the Comparison of Proportions test (*, $P < 0.05$; **, $P < 0.001$; ***, $P < 0.0001$). **(E)** Sequence of

Figure 6. **Transcript and protein levels of DscI are dependent on CortI and IQGAP1 while the transcript level of MyoII is dependent on DscI.**
(A) Western analysis with DscI antibody showed reduction in DscIA protein level in *cortI* and *iqgap1* null mutants. Each cell line was seeded at two different densities 10-fold apart 6 h before analysis. 70 µg of whole cell lysates were loaded on 10% acrylamide gel. Dynacortin (Dyn) is provided as a loading control. **(B)** Quantification of the DscI protein levels after normalization to WT revealed reduced protein expression, particularly in *iqgap1* and *cortI* null cells. Number of

regulated and whose loss or overexpression causes defects to the system. Dynacortin is another example. Dynacortin is a cortical actin-bundling protein whose overexpression leads to defects in growth, cytokinesis fidelity, and cortical mechanics while loss of dynacortin causes altered cell mechanics and cleavage furrow ingression kinetics (Girard et al., 2004; Robinson and Spudich, 2000; Zhang and Robinson, 2005). We are continuously finding that this concept of a sweet spot (not too little, not too much, just right) is a recurring theme in mechanobiology (Schiffhauer et al., 2019).

Furthermore, DscI helps stabilize the interactions between CortI, MyoII, and IQGAP2. These findings lead to a complex mechanistic explanation of the function of DscI in the contractility machinery, in which it acts as part of the mechanoresponsive CKs to fine-tune the accumulation, and hence govern the activity of the contractility machinery at the cortex. In this system, DscI acts as a component of the mechanoreponsive CKs, which function similarly to "packages" that are ready to be delivered to the cortex, where each component is then released. In these packages, DscI can be thought of as a chaperone that helps stabilize the complex and ensure proper delivery of the components, particularly CortI (Fig. 8 B).

Through our prior work, we already had indicators that suggested DscI contributed to the contractility system (Kothari et al., 2019b; Nguyen and Robinson, 2020; Robinson and Spudich, 2000). Interestingly, in our previous FCCS studies (Kothari et al., 2019b), DscI interacted with IQGAP2 only when CortI was present in the cell. In *cortI* null cells, DscI was not detected in the co-immunoprecipitated fraction, foreshadowing the role of CortI in regulating the expression of DscI. We now understand that in *cortI* null cells, DscI expression is reduced at the transcript and protein levels. We also found that DscI not only interacts with key constituents of the mechanoresponsive CKs, but also stabilizes the associations of these proteins with each other. Removing DscI from cells causes a significant decrease in the apparent binding affinities of CortI with MyoII and IQGAP2. Altogether, these results support the notion that DscI functions as part of the CKs and adds a layer of redundancy in regulating the contractility system. These observations are particularly interesting since for decades, DscI has been defined as a secreted/extracellular protein that facilitates membrane–substratum attachment and cell–cell adhesion in developing cells (Bastounis et al., 2016; Huber and O'Day, 2015; Springer et al., 1984). Our work here reveals that DscI also has important functions inside vegetative cells, where DscI remains largely intracellular (Alexander et al., 1992; Clarke et al., 1987). The differential roles of DscI inside and outside of a cell may be partially explained by its differential oligomeric state intracellularly versus extracellularly. DscI remains monomeric in the cytoplasm but assembles into a multimeric (presumably tri- or tetra-meric) state in the secreted multilamellar bodies (Fukuzawa and Ochiai, 1993; Mathieu et al., 2010).

The concept of functional synergy and/or cooperativity is becoming increasingly apparent in contractility systems. MyoII and CortI, the core elements of the mechanoresponsive machinery, both accumulate at the cleavage furrow cortex and exhibit cooperative accumulation at the point of mechanical perturbations. Deletion of one disrupts the stress-dependent accumulation of the other (Kee et al., 2012; Kothari et al., 2019a; Ren et al., 2009). Here, we see a similar story with DscI and IQGAP2. From the genetic interaction analysis, they have a synergistic genetic relationship, indicating that they act in parallel pathways. In this context, the term pathway reflects the genetic interactions. These interactions then help govern the CK complexes that are assembled in the cytoplasm. DscI and IQGAP2 also have common roles in ensuring proper accumulation of CortI at the cortex. In *dscI* null cells, significantly less CortI is found at the interphase cortex. Previously, cells lacking IQGAP2 also had impaired localization of CortI at the cleavage furrow cortex. This redundancy in mechanisms controlling CortI localization adds additional layers of spatial and temporal regulation of the mechanoaccumulation and contractility at the cortex.

Another concept in contractility regulation is that of feedback control, in which the system is structured as a contractility controller that also includes signaling inputs, for example, emanating from the mitotic spindle (Kee et al., 2012; Kothari et al., 2019a; Ren et al., 2009). Multiple modes of regulation through feedback control ensure robust assembly and function of the contractility machinery. While MyoII and CortI sit at the core of the contractility controller as the load-bearing and force-generating proteins, other regulators, such as IQGAP1, IQGAP2, and now DscI, are crucial for ensuring that this system does not over- or under-perform. IQGAP2 binds to CortI and MyoII and acts as positive regulator of this system, permitting the mechanoresponsiveness of these core proteins. To ensure that the system is not overly mechanoresponsive, IQGAP1 antagonizes IQGAP2, thereby controlling CortI and MyoII. As MyoII and CortI actively define the cortical mechanical properties and mechanoresponsiveness, their functions are then tightly regulated and fine-tuned by the feedback control of the IQGAPs (Dickinson et al., 2012; Kee et al., 2012; Pollard and O'Shaughnessy, 2019; Ren et al., 2014). Similarly, DscI fine-tunes CortI cortex levels and helps stabilize the assembly of
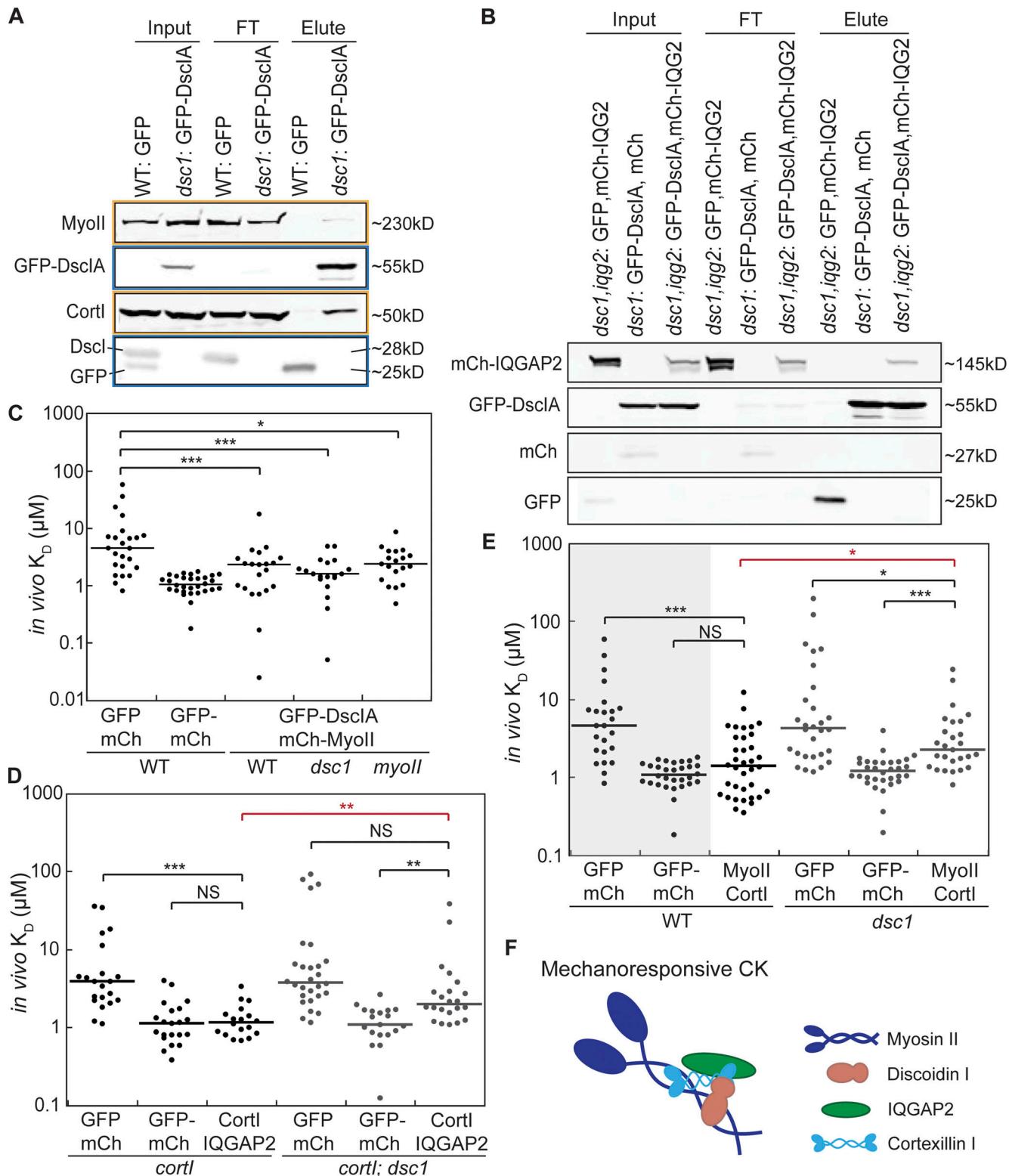
Figure 7. **DscI is a component of the mechanoresponsive CKs. (A and B)** Western blot of co-immunoprecipitation studies of GFP-DscIA in cell lysates of indicated cell lines is shown. FT, flow-through; IQG2, IQGAP2. No antibody for IQGAP2 is available so cell lines expressing mCh-fused IQGAP2 and mouse anti-mCh antibody (Novus Biologicals, 25157SS) were used. In A, bands boxed in the same color (orange or blue) are from the same Western blot. **(C)** Results from FCCS analysis examining interactions between DscIA and MyoII in different cellular backgrounds are shown. The apparent, or in vivo, K_D for unlinked mCherry and GFP (negative control) and fusion GFP-mCherry (positive control) was 5.0 and 1.1 µM, respectively. P values were calculated using the log-transformed data and the ANOVA followed by Fisher's LSD test (*, P < 0.05; ***, P < 0.0001). Number of cells analyzed, n = 19–30 from two independent experiments. **(D)** FCCS analysis confirmed the positive interaction between CortI and IQGAP2 in cortI-complemented background (with an apparent K_D = 1.2; Kothari et al., 2019b). Median in vivo K_Ds for negative (=3.9 and 3.8) and positive (=1.1 and 1.1) controls in cortI-complemented and cortI; dsc1 double mutant background were

similar to that of the WT background (C). In the absence of *dsc1*, CortI and IQGAP2 interacted with an apparent K_D of 2.0, which is significantly weaker than that measured in the presence of DscI. Number of cells analyzed, *n* = 18–28 from two independent experiments. **(E)** FCCS-detected interactions between CortI and MyoII in the WT background (with K_D = 1.5). The affinity between CortI and MyoII was significantly weakened in *dsc1* null mutants (with K_D = 2.6). Positive and negative controls (shaded) in WT background are reproduced from C for direct comparison. Positive and negative controls were also measured in *dsc1* background (in *dsc1*: K_D for negative control = 5.2, K_D for positive control = 1.3). All P values were calculated on the log-transformed data using an Kruskal-Wallis followed by the Wilcoxon test (*, $P < 0.05$; **, $P < 0.001$; ***, $P < 0.0001$). P values signifying the statistical differences in the interactions between the presence and absence of DscI are highlighted in red. Number of cells analyzed, *n* = 24–36 from two independent experiments. **(F)** FCCS data in this study show that DscI helps stabilize the associations between key proteins in the mechanoresponsive CKs. Combined with previous proteomic analysis and co-immunoprecipitation results, it is likely that these proteins, including DscI, function in the same complex, and the absence of one affects the stability of other interactions within the assembly. Source data are available for this figure: SourceData F7.

the mechanoresponsive CKs, and in turn, the expression of DscI is regulated by non-mechanospsonsive CK components. DscI also helps maintain the transcript levels of MyoII, but not protein level, consistent with the fact that many additional levels of regulation control the final protein amount. Nevertheless, this observation suggests that proteins within the cytoskeletal systems have layers of regulation both on transcript and protein levels, rendering its robustness in response to changes or challenges in the system. In an unpublished study, we find an additional major CK component, namely, the RNA-binding protein RNP1A, which binds mRNAs and helps set the levels of transcripts, encoding several cytoskeletal and CK-related proteins.

Overall, the redundancy and feedback control in the cytoskeletal systems allow cells to ensure robust mechanics and mechanoresponsiveness, and high-fidelity shape change such as during cytokinesis.

The discovery and characterization of DscI, a traditional lectin, playing an intracellular function is intriguing, yet not necessarily surprising. In fact, DscI is not the first extracellular lectin protein discovered to have significant intracellular roles. Galectins are prime examples of this. These lectin proteins were first discovered based on their β-galactoside-binding activity and originally implicated in aiding in the formation of complex cell-surface glycans, which help mediate cell–cell recognition
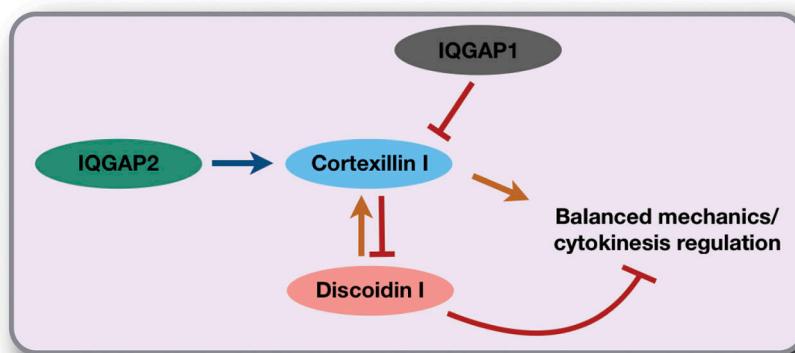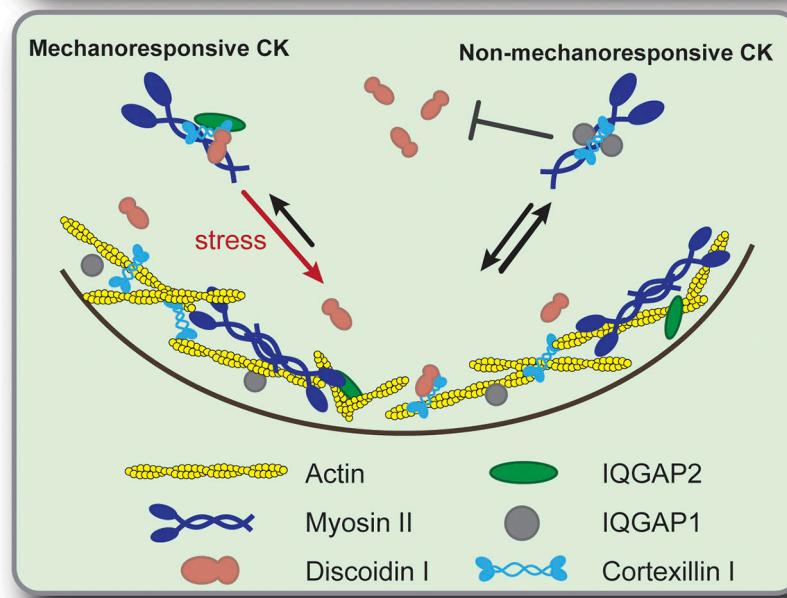
Figure 8. **DscI acts as a modulator of the CK and is regulated by the non-mechanoresponsive CK components. (A)** Schematic depiction of genetic interactions between DscI and key components of the CKs. DscI helps localize CortI to the cortex, which, in turn, is crucial for a balanced cellular mechanics (orange arrows). When components of the non-mechanoresponsive CKs are absent, DscI is deleterious to cytokinesis and is negatively regulated at the mRNA transcript and protein level (red blunt arrows). In contrast, DscI and IQGAP2 act in parallel genetic pathways to maintain normal cytokinesis (orange and blue arrows). **(B)** Mechanistic depiction of DscI intracellular activity and its regulation in the mechanobiome. DscI associates with the mechanoresponsive CK components and helps stabilize their assembly. It also acts to properly localize CortI to the cortex, ensuring WT cortical functions. DscI is negatively regulated by components of the non-mechanoresponsive CKs, which includes IQGAP1.

(Barondes et al., 1994; Johannes et al., 2018; Leffler et al., 2002). However, galectins were later found to reside inside the cell where they contribute to numerous intracellular functions, including having cytoskeletal regulatory roles. For example, Galectin-3 regulates the cytoskeleton through affecting Kras signaling (Reichert and Rotshenker, 2019), and Galectin-8 promotes cytoskeletal rearrangement through activation of Rho in trabecular meshwork cells (Diskin et al., 2012). Moreover, intracellular Galectin-9 sustains the rigidity of cortical actin cytoskeleton, thereby maintaining plasma membrane integrity (Querol Cano et al., 2019). Interestingly, both galectin and dsc proteins have roles as secreted proteins, but neither contain typical signal peptides required for classical secretion. Further, they are lectins that specifically bind to β-galactoside sugars (Cooper, 2002; Mathieu et al., 2010; Vasta et al., 2004; Vasta et al., 2017). The multiple levels of similarity from structures to functions between galectins and discoidins open up new avenues for follow-up studies in deciphering the roles of discoidins and their implications in intracellular function.

Understanding the functions of dsc is providing insights into a broader network that controls and drives the contractility system. Disruption of key proteins in this system often gives rise to aberrant cell behaviors and onsets of diseases (Conti et al., 2015; Nishida et al., 2017; Picariello et al., 2019; Schramek et al., 2014; Surcel et al., 2019). Since the contractility system is implicated in a much broader range of cellular behaviors, additional studies on the roles and functions of DscI in other cellular activities such as migration might lead to additional important findings. Finally, we, and the field, are increasingly finding that many sub-cellular systems are highly integrated, leading to the concept of the contractility machinery plugging into a grander mechanobiome that integrates with diverse cellular systems (Kothari et al., 2019a). Thus, elucidation of the molecular networks that drive this system will undoubtedly provide greater insights into normal cell behaviors as well as many diseases.

Materials and methods
Cell culture and maintenance
A complete list of strains generated and used in this study is provided in Table S1. Cells were grown at 22°C on 10-cm polystyrene plates in Hans' enriched HL-5 media (1.4× HL-5 media with 8% final minimal media, penicillin, and streptomycin). WT-background strains were Ax2 and KAx3. Null mutants utilized were cortI, iqgap2, and iqgap1, and these strains were described in previous studies (Lee et al., 2010; Robinson and Spudich, 2000; Ruppel et al., 1994). Cells were maintained in exponential growth phase and split before reaching maximum confluency. Throughout our experimental designs, we made sure to seed control and mutant cells at the same density for each experiment since DscI expression is density-dependent (Clarke et al., 1987; Jain et al., 1992; Wetterauer et al., 1995).

Cells transformed with protein expression plasmids were grown in enriched 1.4× HL-5 media containing 15 µg/ml G418, 40 µg/ml hygromycin, or a combination of the drugs for double selection. For the agarose overlay assay, cells were maintained in MES buffer (50 mM MES, pH 6.8, 2 mM $MgCl_2$, 0.2 mM $CaCl_2$).

Reagents
Plasmids expressing the following proteins have been previously generated and described: GFP, mCherry, fusion GFP-mCherry, fusion GFP- and/or mCherry-tagged DscIA, CortI, IQGAP1, IQGAP2, and MyoII (Effler et al., 2006; Kee et al., 2012; Lee et al., 2010; West-Foyle et al., 2018; Zhou et al., 2010). For dscIA plasmid generation, dscIA coding sequence obtained from GFP-tagged dscIA pDM181 plasmid was cloned into the pDM181 plasmid between the Sal I and Not I sites. gRNA sequence used for dsc1 gene CRISPR/Cas9 knockout is 5′-AGCATTTATGTGTGT TGCTCTCCA-3′. The transcript level of dscIA was quantified using qRT-PCR with the forward primer 5′-ATGTCTACCCAA GGTTTAGT-3′ and the reverse primer 5′-AAACCACAACCAGCA ACAATGTAT-3′. Both forward and reverse primers recognize regions that are identical in all three dsc1 paralogs (dsc1A, C, and D). The monoclonal mouse antibody 80-52-13 against DscI (cAMP binding domain) and the monoclonal mouse antibody 241-438-1 against cortI, both developed by Günther Gerisch (Max Planck Institute), were obtained from the Developmental Studies Hybridoma Bank (University of Iowa, Iowa City, IA; Stadler et al., 1984). DscI antibody was used at 1:1,000 dilution for Western analysis and at 1:100 dilution for immunocytochemistry. CortI antibody was used at 1:300 dilution for immunocytochemistry. The monoclonal mouse antibody My6 against MyoII heavy chain developed by James Spudich was used at 1:1,000 dilution for immunocytochemistry (Flicker et al., 1985).

RNA isolation and qRT-PCR
Cells were harvested at 5×10^6 cells/ml, and the cell count was determined. Cells were then spinned at 2,000 rpm for 3 min and lysed with 1 ml TRIzol reagent (15596026; Thermo Fisher Scientific) per 1×10^7 cells. 1.6 ml of chloroform was added per 8 ml of TRIzol used, and samples were incubated at room temperature for 3 min. After spinning for 15 min at 3,000 rcf, the top aqueous phase was collected, and RNA was precipitated using isopropyl alcohol. RNA pellets were washed once in 75% ethanol, air-dried, and stored in RNase-free water for qRT-PCR analysis.

qRT-PCR was performed using Verso 1-step RT-qPCR kit (AB4104A). All primer sequences for qRT-PCR analysis are included below. All experiments were conducted on a BIO-RAD CFX Opus 96 Real-Time PCR system. The program used was the following: Reverse Transcription—50°C for 15 min, 95°C for 15 min; PCR—95°C for 15 s, 60°C for 30 s, 72°C for 30 s; melt curve—95°C for 30 s, 60°C for 30 s, and then increased by 0.5°C per 10 s.

Relative quantification of normalized RNA levels was performed using the ΔΔCt method, in which the differences in C_t value between target genes and the control gene GAPDH for each cell line were calculated, and then normalized against WT control cell line.

qRT-PCR primers (used at 200 nM):
For IQGAP1: Forward: 5′-GAAGTCGGTGAACCAGAAGA-3′ and reverse: 5′-CACCTTTGGCAACGAGTGAA-3′.
For IQGAP2: Forward: 5′-GGTTGGGGTAGTGGTATG-3′ and reverse: 5′-CACCGACACACAAGTTAC-3′.
For Dsc1: Forward: 5′-ATGTCTACCCAAGGTTTAGT-3′ and reverse: 5′-AAACCACAACCAGCAACAATGTAT-3′.

For MyoII: Forward: 5′-GCCGATAAGAGTAAGAAGAC-3′ and reverse: 5′-GGATTGTTCAGCTTCAGATT-3′.

For CortI: Forward: 5′-GGCTCGTATGGAACTCAGAG-3′ and reverse: 5′-AAGAGACCAAGACCTTGAGC-3′.

For GAPDH: Forward: 5′-CCCAGAATGTAGAGTTTTAG-3′ and reverse: 5′-CTACAATGTATTCAGCACC-3′.

Plasmid transformation and exogenous protein expression

Cells were harvested during the exponential growth phase on plates and washed once with ice-cold E-Pore buffer. Cells are then suspended in cold E-Pore buffer at a concentration of 0.5–1.0 × 10^7 cells/ml. A mixture containing 1–4 µg of plasmid and 350 µl of suspended cells was transferred to a cold 4-mm electroporation cuvette. Electroporation was performed by one pulse using Genepulser-II electroporator (Bio-Rad) at 1.1 kV and 3.0 µF capacitance. Pulsed cells were transferred to a Petri dish containing 10 ml of cold Hans' enriched HL-5 media. After 8–16 h, cells were placed in corresponding drug media for transformant selection. Colonies of transformants should appear around 6 d after electroporation. Protein expression was verified using fluorescence imaging and/or Western analysis.

CRISPR/Cas9 to generate KO mutants

A detailed protocol for using CRISPR/Cas9 system to target specific genes and generate KO mutants in *D. discoideum* is described in Sekine et al. (2018). gRNA guide sequences targeting *dsc1* gene were designed using Cas-Designer. The gRNA sequence is detailed in the Reagents section. Customized gRNA oligos were obtained from Integrated DNA Technologies. This selected gRNA sequence is complementary to a 24 nt-long *dsc1* coding region near the 3′ end that is identical in all three *dsc1* paralogs (*dsc1A, C*, and *D*). gRNA sequence was then cloned into pTM1285 plasmid obtained from NBRP Nenkin.

Background cells were transformed with pTM1285 plasmid containing *dsc1* gRNA using electroporation, using the transformation protocol described above. After 8–16 h of transformation, we replaced the media with Hans' enriched HL-5 media containing 15 µg of G418 and cultured the transformed cells for 3 more days. After that, floating dead cells were washed off with Hans' enriched HL-5 media. Remaining live cells were plated on SM-5 plates with cultured *Klebsiella aerogenes* and incubated at room temperature for 3–4 d until visible, isolated plaques formed. These individual plaques were separately transferred to 48-well plates containing Hans' enriched HL-5 media in the absence of G418. After approximately 2–3 d when colonies grew, they were transferred to 10-cm Petri dishes. Since the cells should be expressing Cas9 and gRNA only transiently, it was important to test a subpopulation of these cells for G418 sensitivity to ensure the absence of pTM1285 plasmid. Retainment of the plasmid can potentially induce off-target gene modifications.

Suspension growth assay

Cells were seeded in 10 ml Hans' enriched HL-5 media in 150-ml Erlenmeyer flasks at a starting cell concentration of 1.0 × 10^5 cells/ml. The flasks were rotated on a shaker at 180 rpm in a 22°C incubator. Cell concentration was measured and recorded roughly every 24 h using a hemocytometer. It is important to note that because of the time lag required for the winner cells to populate the cultures, we normally acquire and analyze data from a second cycle of suspension culture. As cells reached the later point of exponential growth phase, they were split down to a concentration of 0.5 – 1 × 10^5 cells/ml. Afterwards, the cell density continued to be measured and recorded roughly every 24 h (the exact time was recorded).

Relative growth rates were determined by plotting cell densities versus time. The exponential phase curve from the second cycle was fitted to a single exponential equation using Kaleida-Graph (Synergy Software). Growth rates (r) were determined for each growth curve using the exponential growth equation:

$$n(t) = n_0 e^{rt},$$

where n(t) = population at time t, n_O = initial population concentration, r = relative growth rate, and t = time.

Multinucleation assay

Cells that have been in suspension at 180 rpm for 2–3 d were seeded at ~70% confluency on glass coverslips in Hans' enriched HL-5 media and allowed to adhere for 15–30 min. Next, media was removed, and cells were fixed with ice-cold fixative solution (2% PFA + 0.01% Triton X-100 in 1.5× HL-5 media) for 10 min. They were then washed quickly with 1× PBS, and the nuclei were stained with 10 µg/ml Hoechst for 10 min. Afterwards, cells were washed three times, 10 min each time, with 1× PBT (1× PBS + 0.01% Triton X-100). Before visualization, cells were mounted on coverslips using Invitrogen Prolong Diamond Antifade Mountan. Cells were imaged using a MolDev ImageXpress High-content Imager, equipped with a 10× dry objective (NA 0.25), and the number of nuclei per cell was recorded for 100–200 cells.

MPA, effective cortical tension, and mechanoresponsiveness quantification

A more detailed and thorough MPA setup was described in our previous review (Kee and Robinson, 2013). In short, micropipettes of ~5 µm diameter (exact diameter is measured for each pipette during use) were stabilized at the bottom of the cell chamber. Exponential growth phase cells were seeded in imaging chambers at ~10% confluency. Small aspiration pressure was generated to form attachment between the cell and the pipette tip. The aspiration pressure was then increased to the equilibrium pressure (ΔP) at which the length of the cell inside the pipette (L_p) is equal to the radius of the pipette (R_p). The cell was released at this point and allowed to rest for a few minutes before a second measurement was made. Effective cortical tension for each individual cell was measured as the average of the two independent measurements of that cell. Effective cortical tension was quantified using the Young-Laplace equation:

$$\Delta P = 2T_{eff}\left(\frac{1}{R_p} - \frac{1}{R_c}\right),$$

where ΔP = aspiration pressure that produced a deformation where L_p = R_p, T_{eff} = effective cortical tension, R_p = radius of the pipette, and R_c = radius of the cell outside the pipette.

For the mechanoresponsiveness measurement, cells at exponential growth phase were slowly aspirated to ~0.80 nN/µm²

and held for at least 100 s. For quantification, the ratio of the background-corrected mean signal intensity of the cortex inside the pipette (I_p) to that of the opposite cortex outside the pipette (I_o) was calculated.

Western blot quantification

Nitrocellulose membranes were imaged using 700- and 800-nm laser channels with the auto-exposure feature on Li-COR OD-YSSEY CLx system. The blot images contain 16-bit data, allowing for a wide dynamic range in the signal. A rectangular shape was drawn around each protein band, and these bands were quantified using the integrated density measurement and normalized against the background signal. These values were then normalized against the corresponding Dynacortin band values. In some experiments, the normalized protein expression values were normalized against the respective control, typically a WT parental control, and plotted on a dotplot.

Agarose compression assay

Thin sheets of 2% agarose gel in MES buffer (recipe above) were prepared as described previously (Kee et al., 2012; Miao et al., 2017). Agarose sheets were cut into small pieces that fit inside an 8-well chamber. Cells were seeded at an equal density of 1 × 10⁶ cells/ml in 8-well imaging chambers, which led to ~70% confluency. Cells were then allowed to adhere for 30 min. Cell media was replaced with MES buffer. Afterwards, the agarose sheet was carefully placed inside the chamber on top of the cells. MES buffer was slowly aspirated from the chamber, allowing the agarose sheet to gradually press on the cells. Cells were imaged using an Olympus IX71 microscope, equipped with a 40× (NA 1.30) oil objective, at room temperature, immediately to avoid evaporation and any further complications caused by extended compression. Images were acquired with DIC and GFP channels using Metamorph software, and then analyzed using ImageJ.

Immunocytochemistry

Cells were seeded at an equal density of 1 × 10⁶ cells/ml on a detachable 8-well chamber slide and allowed to adhere for 30 min. Media was removed and cells were fixed in –20°C methanol for 3 min. Residual methanol was quickly washed with 1× PBT (1× PBS + 0.05% Triton X-100), and cells were blocked in blocking buffer (3% BSA in 1× PBS) for 1 h at room temperature. Proteins of interest were detected using corresponding primary antibodies diluted in blocking buffer for 1–3 h at room temperature. Afterwards, cells were washed three times with 1× PBT (1× PBS + 0.05% Triton X-100), followed by room temperature incubation with appropriate secondary antibodies for 1 h. For nuclei detection, cells were washed once with 1× PBS and stained with 1 μg/ml Hoescht for 10 min. Cells were then washed three times, 10 min each time, with 1× PBT. Before visualization, cells were mounted on coverslips using Invitrogen Prolong Diamond Antifade Mountant.

FCCS

A more detailed and thorough FCCS setup was described in our previous studies (Kothari et al., 2017; Srivastava and Robinson, 2015; West-Foyle et al., 2018). Fluorescent protein-expressing cells were imaged using a Zeiss AxioObserver with 780-Quasar confocal module microscope, equipped with a C-Apochromat 40× (NA 1.2) water objective. Images were acquired using Zen software with mCherry and GFP channels. 100 nM Rhodamine 6G was used for pinhole alignment, Z-plane determination, and laser power calibration. Cells with high fluorescence signal intensity were avoided for this measurement to avoid fluorophore saturation. Fluorescence intensity data of two fluorophores were fitted to a single-component 3D diffusion model with a triplet-state component. The in vivo K_D values were calculated using the following equation (previously described in Srivastava and Robinson [2015]):

$$invivoK_D = \left(\frac{G_x}{N.V.G_a.G_b}\right) \cdot \left(\frac{G_a}{G_x} - 1\right) \cdot \left(\frac{G_b}{G_x} - 1\right),$$

where G_x = cross-correlation of two fluorophores, G_a = auto-correlation for mCherry, G_b = auto-correlation for GFP, N = Avogadro's number, and V = confocal volume.

Co-immunoprecipitation of GFP-DscIA

Approximately 3 × 10⁷ logarithmically growing cells were harvested, washed once in 1× PBS, and resuspended in 300 μl of freshly made lysis buffer (100 mM PIPES, pH 6.8, 2.5 mM EGTA, 1 mM MgCl₂, 1 mM ATP, 0.1% Triton X-100, 100 mM NaCl, and protease inhibitor cocktail). Cell lysates were incubated on ice for 30 min, with gentle inversion every 10 min. Lysates were then centrifuged at 15,000 g for 5 min at 4°C. The supernatant was diluted with 200 μl dilution buffer (100 mM PIPES, pH 6.8, 2.5 mM EGTA, 1 mM MgCl₂, 1 mM ATP, 100 mM NaCl, and protease inhibitor cocktail). 50 μl of the diluted lysates were saved as Input. Diluted lysates were then transferred to tubes containing 25 μl of GFP-trap agarose beads (Chromotek gta-10) and rotated at 4°C for 1 h. These beads were previously equilibrated according to the manufacturer's instructions. Afterwards, beads were sedimented by centrifugation at 2,500 g for 5 min. 50 μl of the supernatant was saved as flow-through and the rest was discarded. Beads were washed two times in 500 μl wash buffer (dilution buffer + 0.01% Triton X-100). Beads were then resuspended in 70 μl 2× sample suffer plus 10% β-mercaptoethanol and boiled at 95°C for 5 min. Beads were sedimented at 2,500 g for 2 min, and samples were transferred to another tube. Approximately 30 μl of dilution buffer was added to final samples to bring the sample buffer to 1×. 50 μl 2× sample buffer plus 10% β-mercaptoethanol was added to each input and flow-through fraction and boiled at 95°C for 5 min. 20 μl of each sample was loaded on a Western gel for analysis.

Statistical analysis

Data sets that appeared to be normally distributed (but this was not formally tested) were statistically analyzed using ANOVA followed by Fisher's least significant difference (LSD) test. Calculated P values that are lower than or equal to 0.05 were considered to be statistically significant. Data sets that were skewed and/or contained significant outliers were statistically analyzed using the Kruskal–Wallis test followed by the Mann-Whitney-Wilcoxon test. P values are either provided in each graph or denoted as *, $P < 0.05$; **, $P < 0.001$; ***, $P < 0.0001$. The

above statistical tests were performed using the statistical test functions provided by Kaleidagraph. For data sets that considered differences in proportions (fractions), the Comparison of Proportions test was used (http://medcalc.org).

Online supplemental material
Supplemental materials include Figs. S1, S2, S3, S4, and S5, Tables S1 and S2, and Videos 1, 2, 3, 4, and 5. Fig. S1 shows cytokinetic defects in *dsc1* null mutants generated in the Ax2 background. Fig. S2 shows exogenous expression of DscIA rescues cytokinetic defects of *dsc1* null mutants. Fig. S3 shows the absence of DscI in the cell has no effect on the cortical localization of Myosin II and IQGAP2. Fig. S4 shows that DscI facilitates CortI's cleavage furrow accumulation. Fig. S5 shows DscIA has antagonistic genetic interactions with CortI and IQGAP1 and synergistic genetic interactions with IQGAP2. Table S1 provides a summary of all *D. discoideum* cell strains used in this study. Table S2 provides growth rates of background and null-complemented cell lines used in the genetic interaction assays. Videos 1, 2, 3, 4, and 5 show dividing WT (KAx3), *dsc1* null, *dsc1*:GFP-DscIA, *iqgap2* null, and *iqgap2; dsc1* null cells, respectively.

Data availability
Cell lines and reagents generated in this study will be made available to the scientific community upon request.

References
Adachi, H. 2001. Identification of proteins involved in cytokinesis of Dictyostelium. *Cell Struct. Funct.* 26:571–575. https://doi.org/10.1247/csf.26.571

Adachi, H., Y. Takahashi, T. Hasebe, M. Shirouzu, S. Yokoyama, and K. Sutoh. 1997. Dictyostelium IQGAP-related protein specifically involved in the completion of cytokinesis. *J. Cell Biol.* 137:891–898. https://doi.org/10.1083/jcb.137.4.891

Alexander, S., T.M. Shinnick, and R.A. Lerner. 1983. Mutants of *Dictyostelium discoideum* blocked in expression of all members of the developmentally regulated discoidin multigene family. *Cell.* 34:467–475. https://doi.org/10.1016/0092-8674(83)90380-x

Alexander, S., L.M. Sydow, D. Wessels, and D.R. Soll. 1992. Discoidin proteins of *Dictyostelium* are necessary for normal cytoskeletal organization and cellular morphology during aggregation. *Differentiation.* 51:149–161. https://doi.org/10.1111/j.1432-0436.1992.tb00691.x

Bacia, K., S.A. Kim, and P. Schwille. 2006. Fluorescence cross-correlation spectroscopy in living cells. *Nat. Methods.* 3:83–89. https://doi.org/10.1038/nmeth822

Barai, A., A. Mukherjee, A. Das, N. Saxena, and S. Sen. 2021. α-Actinin-4 drives invasiveness by regulating myosin IIB expression and myosin IIA localization. *J. Cell Sci.* 134:jcs258581. https://doi.org/10.1242/jcs.258581

Barondes, S.H., D.N. Cooper, M.A. Gitt, and H. Leffler. 1994. Galectins—structure and function of a large family of animal lectins. *J. Biol. Chem.* 269:20807–20810. https://doi.org/10.1016/s0021-9258(17)31891-4

Barondes, S.H., P.L. Haywood-Reid, and D.N. Cooper. 1985. Discoidin I, an endogenous lectin, is externalized from *Dictyostelium discoideum* in multilamellar bodies. *J. Cell Biol.* 100:1825–1833. https://doi.org/10.1083/jcb.100.6.1825

Bastounis, E., B. Alvarez-Gonzalez, J.C. del Alamo, J.C. Lasheras, and R.A. Firtel. 2016. Cooperative cell motility during tandem locomotion of amoeboid cells. *Mol. Biol. Cell.* 27:1262–1271. https://doi.org/10.1091/mbc.E15-12-0836

Baumgartner, S., K. Hofmann, R. Chiquet-Ehrismann, and P. Bucher. 1998. The discoidin domain family revisited: New members from prokaryotes and a homology-based fold prediction. *Protein Sci.* 7:1626–1631. https://doi.org/10.1002/pro.5560070717

Berger, E.A., and D.R. Armant. 1982. Discoidins I and II: Common and unique regions on two lectins implicated in cell--cell cohesion in *Dictyostelium discoideum. Proc. Natl. Acad. Sci. USA.* 79:2162–2166. https://doi.org/10.1073/pnas.79.7.2162

Blanchoin, L., R. Boujemaa-Paterski, C. Sykes, and J. Plastino. 2014. Actin dynamics, architecture, and mechanics in cell motility. *Physiol. Rev.* 94:235–263. https://doi.org/10.1152/physrev.00018.2013

Brill, S., S. Li, C.W. Lyman, D.M. Church, J.J. Wasmuth, L. Weissbach, A. Bernards, and A.J. Snijders. 1996. The Ras GTPase-activating-protein-related human protein IQGAP2 harbors a potential actin binding domain and interacts with calmodulin and Rho family GTPases. *Mol. Cell. Biol.* 16:4869–4878. https://doi.org/10.1128/MCB.16.9.4869

Charras, G.T., C.K. Hu, M. Coughlin, and T.J. Mitchison. 2006. Reassembly of contractile actin cortex in cell blebs. *J. Cell Biol.* 175:477–490. https://doi.org/10.1083/jcb.200602085

Chikina, A.S., T.M. Svitkina, and A.Y. Alexandrova. 2019. Time-resolved ultrastructure of the cortical actin cytoskeleton in dynamic membrane blebs. *J. Cell Biol.* 218:445–454. https://doi.org/10.1083/jcb.201806075

Clarke, M., S.C. Kayman, and K. Riley. 1987. Density-dependent induction of discoidin-I synthesis in exponentially growing cells of *Dictyostelium discoideum. Differentiation.* 34:79–87. https://doi.org/10.1111/j.1432-0436.1987.tb00053.x

Conti, M.A., A.D. Saleh, L.R. Brinster, H. Cheng, Z. Chen, S. Cornelius, C. Liu, X. Ma, C. Van Waes, and R.S. Adelstein. 2015. Conditional deletion of nonmuscle myosin II-A in mouse tongue epithelium results in squamous cell carcinoma. *Sci. Rep.* 5:14068. https://doi.org/10.1038/srep14068

Cooper, D.N. 2002. Galectinomics: Finding themes in complexity. *Biochim. Biophys. Acta.* 1572:209–231. https://doi.org/10.1016/s0304-4165(02)00310-0

Dickinson, D.J., D.N. Robinson, W.J. Nelson, and W.I. Weis. 2012. alpha-catenin and IQGAP regulate myosin localization to control epithelial tube morphogenesis in *Dictyostelium. Dev. Cell.* 23:533–546. https://doi.org/10.1016/j.devcel.2012.06.008

Diskin, S., W.-S. Chen, Z. Cao, S. Gyawali, H. Gong, A. Soza, A. González, and N. Panjwani. 2012. Galectin-8 promotes cytoskeletal rearrangement in trabecular meshwork cells through activation of Rho signaling. *PLoS One.* 7(9):e44400. https://doi.org/10.1371/journal.pone.0044400

Effler, J.C., Y.S. Kee, J.M. Berk, M.N. Tran, P.A. Iglesias, and D.N. Robinson. 2006. Mitosis-specific mechanosensing and contractile-protein redistribution control cell shape. *Curr. Biol.* 16:1962–1967. https://doi.org/10.1016/j.cub.2006.08.027

Efremov, Y.M., A.A. Dokrunova, A.V. Efremenko, M.P. Kirpichnikov, K.V. Shaitan, and O.S. Sokolova. 2015. Distinct impact of targeted actin cytoskeleton reorganization on mechanical properties of normal and malignant cells. *Biochim. Biophys. Acta.* 1853:3117–3125. https://doi.org/10.1016/j.bbamcr.2015.05.008

Faix, J., I. Weber, U. Mintert, J. Kohler, F. Lottspeich, and G. Marriott. 2001. Recruitment of cortexillin into the cleavage furrow is controlled by Rac1

and IQGAP-related proteins. *EMBO J.* 20:3705–3715. https://doi.org/10.1093/emboj/20.14.3705

Flicker, P.F., G. Peltz, M.P. Sheetz, P. Parham, and J.A. Spudich. 1985. Site-specific inhibition of myosin-mediated motility in vitro by monoclonal antibodies. *J. Cell Biol.* 100:1024–1030. https://doi.org/10.1083/jcb.100.4.1024

Frazier, W.A., S.D. Rosen, R.W. Reitherman, and S.H. Barondes. 1975. Purification and comparison of two developmentally regulated lectins from Dictyostelium discoideum. Discoidin I and II. *J. Biol. Chem.* 250: 7714–7721. https://doi.org/10.1016/s0021-9258(19)40874-0

Fritzsche, M., C. Erlenkamper, E. Moeendarbary, G. Charras, and K. Kruse. 2016. Actin kinetics shapes cortical network structure and mechanics. *Sci. Adv.* 2:e1501337. https://doi.org/10.1126/sciadv.1501337

Fukuzawa, M., and H. Ochiai. 1993. Different subcellular localizations of discoidin I monomer and tetramer in Dictyostelium discoideum cells: Using conformation-specific monoclonal antibodies. *Exp. Cell Res.* 204: 61–72. https://doi.org/10.1006/excr.1993.1009

Ghosh, I., R.K. Singh, M. Mishra, S. Kapoor, and S.S. Jana. 2021. Switching between blebbing and lamellipodia depends on the degree of non-muscle myosin II activity. *J. Cell Sci.* 134:jcs248732. https://doi.org/10.1242/jcs.248732

Girard, K.D., C. Chaney, M. Delannoy, S.C. Kuo, and D.N. Robinson. 2004. Dynacortin contributes to cortical viscoelasticity and helps define the shape changes of cytokinesis. *EMBO J.* 23:1536–1546. https://doi.org/10.1038/sj.emboj.7600167

Hart, M.J., M.G. Callow, B. Souza, and P. Polakis. 1996. IQGAP1, a calmodulin-binding protein with a rasGAP-related domain, is a potential effector for cdc42Hs. *EMBO J.* 15:2997–3005. https://doi.org/10.1002/j.1460-2075.1996.tb00663.x

Huber, R.J., and D.H. O'Day. 2015. Proteomic profiling of the extracellular matrix (slime sheath) of Dictyostelium discoideum. *Proteomics.* 15: 3315–3319. https://doi.org/10.1002/pmic.201500143

Jain, R., I.S. Yuen, C.R. Taphouse, and R.H. Gomer. 1992. A density-sensing factor controls development in *Dictyostelium*. *Genes Dev.* 6:390–400. https://doi.org/10.1101/gad.6.3.390

Johannes, L., R. Jacob, and H. Leffler. 2018. Galectins at a glance. *J. Cell Sci.* 131: jcs208884. https://doi.org/10.1242/jcs.208884

Kee, Y.S., Y. Ren, D. Dorfman, M. Iijima, R. Firtel, P.A. Iglesias, and D.N. Robinson. 2012. A mechanosensory system governs myosin II accumulation in dividing cells. *Mol. Biol. Cell.* 23:1510–1523. https://doi.org/10.1091/mbc.E11-07-0601

Kee, Y.S., and D.N. Robinson. 2013. Micropipette aspiration for studying cellular mechanosensory responses and mechanics. *Methods Mol. Biol.* 983:367–382. https://doi.org/10.1007/978-1-62703-302-2_20

Kiedzierska, A., K. Smietana, H. Czepczynska, and J. Otlewski. 2007. Structural similarities and functional diversity of eukaryotic discoidin-like domains. *Biochim. Biophys. Acta.* 1774:1069–1078. https://doi.org/10.1016/j.bbapap.2007.07.007

Kothari, P., C. Johnson, C. Sandone, P.A. Iglesias, and D.N. Robinson. 2019a. How the mechanobiome drives cell behavior, viewed through the lens of control theory. *J. Cell Sci.* 132:jcs234476. https://doi.org/10.1242/jcs.234476

Kothari, P., E.S. Schiffhauer, and D.N. Robinson. 2017. Cytokinesis from nanometers to micrometers and microseconds to minutes. *Methods Cell Biol.* 137:307–322. https://doi.org/10.1016/bs.mcb.2016.03.038

Kothari, P., V. Srivastava, V. Aggarwal, I. Tchernyshyov, J.E. Van Eyk, T. Ha, and D.N. Robinson. 2019b. Contractility kits promote assembly of the mechanoresponsive cytoskeletal network. *J. Cell Sci.* 132:jcs226704. https://doi.org/10.1242/jcs.226704

Lee, S., Z. Shen, D.N. Robinson, S. Briggs, and R.A. Firtel. 2010. Involvement of the cytoskeleton in controlling leading-edge function during chemotaxis. *Mol. Biol. Cell.* 21:1810–1824. https://doi.org/10.1091/mbc.e10-01-0009

Leffler, H., S. Carlsson, M. Hedlund, Y. Qian, and F. Poirier. 2002. Introduction to galectins. *Glycoconj. J.* 19:433–440. https://doi.org/10.1023/B:GLYC.0000014072.34840.04

Liu, Y., and D. Robinson. 2018. Recent advances in cytokinesis: Understanding the molecular underpinnings. *F1000Res.* 7:F1000. https://doi.org/10.12688/f1000research.16502.1

Luo, T., K. Mohan, V. Srivastava, Y. Ren, P.A. Iglesias, and D.N. Robinson. 2012. Understanding the cooperative interaction between myosin II and actin cross-linkers mediated by actin filaments during mechanosensation. *Biophys. J.* 102:238–247. https://doi.org/10.1016/j.bpj.2011.12.020

Luo, T., and D.N. Robinson. 2011. The role of the actin cytoskeleton in mechanosensation. In *Mechanosensitivity in Cells and Tissues 4: Mechanosensitivity*

and Mechanotransduction. A. Kamkin, and I. Kiseleva, editors. Springer-Verlag, New York. 25–65

Mathieu, S.V., K.S. Aragao, A. Imberty, and A. Varrot. 2010. Discoidin I from Dictyostelium discoideum and interactions with oligosaccharides: Specificity, affinity, crystal structures, and comparison with discoidin II. *J. Mol. Biol.* 400:540–554. https://doi.org/10.1016/j.jmb.2010.05.042

Miao, C., E.S. Schiffhauer, E.I. Okeke, D.N. Robinson, and T. Luo. 2017. Parallel compression is a fast low-cost assay for the high-throughput screening of mechanosensory cytoskeletal proteins in cells. *ACS Appl. Mater. Interfaces.* 9:28168–28179. https://doi.org/10.1021/acsami.7b04622

Mondal, S., B. Burgute, D. Rieger, R. Muller, F. Rivero, J. Faix, M. Schleicher, and A.A. Noegel. 2010. Regulation of the actin cytoskeleton by an interaction of IQGAP related protein GAPA with filamin and cortexillin I. *PLoS One.* 5:e15440. https://doi.org/10.1371/journal.pone.0015440

Murthy, K., and P. Wadsworth. 2005. Myosin-II-dependent localization and dynamics of F-actin during cytokinesis. *Curr. Biol.* 15:724–731. https://doi.org/10.1016/j.cub.2005.02.055

Neujahr, R., C. Heizer, and G. Gerisch. 1997. Myosin II-independent processes in mitotic cells of *Dictyostelium discoideum*: Redistribution of the nuclei, re-arrangement of the actin system and formation of the cleavage furrow. *J. Cell Sci.* 110 (Pt 2):123–137. https://doi.org/10.1242/jcs.110.2.123

Nguyen, L.T.S., M.A.C. Jacob, E. Parajon, and D.N. Robinson. 2022. Cancer as a biophysical disease: Targeting the mechanical-adaptability program. *Biophys. J.* S0006-3495:00367-00368. https://doi.org/10.1016/j.bpj.2022.04.039

Nguyen, L.T.S., and D.N. Robinson. 2020. The unusual suspects in cytokinesis: Fitting the pieces together. *Front. Cell Dev. Biol.* 8:441. https://doi.org/10.3389/fcell.2020.00441

Nishida, K., K.A. Brune, N. Putcha, P. Mandke, W.K. O'Neal, D. Shade, V. Srivastava, M. Wang, H. Lam, S.S. An, et al. 2017. Cigarette smoke disrupts monolayer integrity by altering epithelial cell-cell adhesion and cortical tension. *Am. J. Physiol. Lung Cell Mol. Physiol.* 313:L581–L591. https://doi.org/10.1152/ajplung.00074.2017

Park, B., H. Kim, and T.J. Jeon. 2018. Loss of RapC causes defects in cytokinesis, cell migration, and multicellular development of *Dictyostelium*. *Biochem. Biophys. Res. Commun.* 499:783–789. https://doi.org/10.1016/j.bbrc.2018.03.223

Picariello, H.S., R.S. Kenchappa, V. Rai, J.F. Crish, A. Dovas, K. Pogoda, M. McMahon, E.S. Bell, U. Chandrasekharan, A. Luu, et al. 2019. Myosin IIA suppresses glioblastoma development in a mechanically sensitive manner. *Proc. Natl. Acad. Sci. USA.* 116:15550–15559. https://doi.org/10.1073/pnas.1902847116

Pollard, T.D., and B. O'Shaughnessy. 2019. Molecular mechanism of cytokinesis. *Annu. Rev. Biochem.* 88:661–689. https://doi.org/10.1146/annurev-biochem-062917-012530

Querol Cano, L., O. Tagit, Y. Dolen, A. van Duffelen, S. Dieltjes, S.I. Buschow, T. Niki, M. Hirashima, B. Joosten, K. van den Dries, et al. 2019. Intracellular galectin-9 controls dendritic cell function by maintaining plasma membrane rigidity. *iScience.* 22:240–255. https://doi.org/10.1016/j.isci.2019.11.019

Rao, X., X. Huang, Z. Zhou, and X. Lin. 2013. An improvement of the 2(-delta delta CT) method for quantitative real-time polymerase chain reaction data analysis. *Biostat. Bioinforma. Biomath.* 3:71–85

Reichert, F., and S. Rotshenker. 2019. Galectin-3 (MAC-2) Controls Microglia Phenotype Whether Amoeboid and Phagocytic or Branched and Non-phagocytic by Regulating the Cytoskeleton. *Front Cell Neurosci.* 13:90. https://doi.org/10.3389/fncel.2019.00090

Ren, Y., J.C. Effler, M. Norstrom, T. Luo, R.A. Firtel, P.A. Iglesias, R.S. Rock, and D.N. Robinson. 2009. Mechanosensing through cooperative interactions between myosin II and the actin crosslinker cortexillin I. *Curr. Biol.* 19:1421–1428. https://doi.org/10.1016/j.cub.2009.07.018

Ren, Y., H. West-Foyle, A. Surcel, C. Miller, and D.N. Robinson. 2014. Genetic suppression of a phosphomimic myosin II identifies system-level factors that promote myosin II cleavage furrow accumulation. *Mol. Biol. Cell.* 25:4150–4165. https://doi.org/10.1091/mbc.E14-08-1322

Rivero, F., D. Illenberger, B.P. Somesh, H. Dislich, N. Adam, and A.K. Meyer. 2002. Defects in cytokinesis, actin reorganization and the contractile vacuole in cells deficient in RhoGDI. *EMBO J.* 21:4539–4549. https://doi.org/10.1093/emboj/cdf449

Robinson, D.N., and J.A. Spudich. 2000. Dynacortin, a genetic link between equatorial contractility and global shape control discovered by library complementation of a *Dictyostelium discoideum* cytokinesis mutant. *J. Cell Biol.* 150:823–838. https://doi.org/10.1083/jcb.150.4.823

Rosen, S.D., J.A. Kafka, D.L. Simpson, and S.H. Barondes. 1973. Developmentally regulated, carbohydrate-binding protein in *Dictyostelium discoideum*. *Proc. Natl. Acad. Sci. USA*. 70:2554–2557. https://doi.org/10.1073/pnas.70.9.2554

Ruppel, K.M., T.Q. Uyeda, and J.A. Spudich. 1994. Role of highly conserved lysine 130 of myosin motor domain. In vivo and in vitro characterization of site specifically mutated myosin. *J. Biol. Chem.* 269:18773–18780. https://doi.org/10.1016/s0021-9258(17)32235-4

Schiffhauer, E.S., T.Z. Luo, K. Mohan, X.Y. Qian, V. Srivastava, P. Iglesias, and D.N. Robinson. 2017. Mechanoaccumulative elements of the mammalian actin cytoskeleton. *Biophys. J.* 112:268a. https://doi.org/10.1016/j.bpj.2016.11.1456

Schiffhauer, E.S., Y. Ren, V.A. Iglesias, P. Kothari, P.A. Iglesias, and D.N. Robinson. 2019. Myosin IIB assembly state determines its mechanosensitive dynamics. *J. Cell Biol.* 218:895–908. https://doi.org/10.1083/jcb.201806058

Schramek, D., A. Sendoel, J.P. Segal, S. Beronja, E. Heller, D. Oristian, B. Reva, and E. Fuchs. 2014. Direct in vivo RNAi screen unveils myosin IIa as a tumor suppressor of squamous cell carcinomas. *Science.* 343:309–313. https://doi.org/10.1126/science.1248627

Sekine, R., T. Kawata, and T. Muramoto. 2018. CRISPR/Cas9 mediated targeting of multiple genes in *Dictyostelium*. *Sci. Rep.* 8:8471. https://doi.org/10.1038/s41598-018-26756-z

Simson, R., E. Wallraff, J. Faix, J. Niewohner, G. Gerisch, and E. Sackmann. 1998. Membrane bending modulus and adhesion energy of wild-type and mutant cells of *Dictyostelium* lacking talin or cortexillins. *Biophys. J.* 74:514–522. https://doi.org/10.1016/S0006-3495(98)77808-7

Sinha, R., N. Verdonschot, B. Koopman, and J. Rouwkema. 2017. Tuning cell and tissue development by combining multiple mechanical signals. *Tissue Eng. B Rev.* 23:494–504. https://doi.org/10.1089/ten.TEB.2016.0500

Springer, W.R., and S.H. Barondes. 1980. Cell adhesion molecules: Detection with univalent second antibody. *J. Cell Biol.* 87:703–707. https://doi.org/10.1083/jcb.87.3.703

Springer, W.R., D.N. Cooper, and S.H. Barondes. 1984. Discoidin I is implicated in cell-substratum attachment and ordered cell migration of Dictyostelium discoideum and resembles fibronectin. *Cell.* 39:557–564. https://doi.org/10.1016/0092-8674(84)90462-8

Srivastava, V., P.A. Iglesias, and D.N. Robinson. 2016. Cytokinesis: Robust cell shape regulation. *Semin. Cell Dev. Biol.* 53:39–44. https://doi.org/10.1016/j.semcdb.2015.10.023

Srivastava, V., and D.N. Robinson. 2015. Mechanical stress and network structure drive protein dynamics during cytokinesis. *Curr. Biol.* 25:663–670. https://doi.org/10.1016/j.cub.2015.01.025

Stadler, J., G. Bauer, M. Westphal, and G. Gerisch. 1984. Monoclonal antibody against cytoplasmic lectins of *Dictyostelium discoideum*: Cross-reactivity with a membrane glycoprotein, contact site A, and with E. coli beta-galactosidase and lac repressor. *Hoppe Seylers Z. Physiol. Chem.* 365:283–288. https://doi.org/10.1515/bchm2.1984.365.1.283

Stock, A., M.O. Steinmetz, P.A. Janmey, U. Aebi, G. Gerisch, R.A. Kammerer, I. Weber, and J. Faix. 1999. Domain analysis of cortexillin I: Actin-bundling, PIP(2)-binding and the rescue of cytokinesis. *EMBO J.* 18:5274–5284. https://doi.org/10.1093/emboj/18.19.5274

Surcel, A., E.S. Schiffhauer, D.G. Thomas, Q. Zhu, K.T. DiNapoli, M. Herbig, O. Otto, H. West-Foyle, A. Jacobi, M. Krater, et al. 2019. Targeting mechanoresponsive proteins in pancreatic cancer: 4-Hydroxyacetophenone blocks dissemination and invasion by activating MYH14. *Cancer Res.* 79:4665–4678. https://doi.org/10.1158/0008-5472.CAN-18-3131

Umbarger, H.E. 1956. Evidence for a negative-feedback mechanism in the biosynthesis of isoleucine. *Science.* 123:848. https://doi.org/10.1126/science.123.3202.848

Uyeda, T.Q., C. Kitayama, and S. Yumura. 2000. Myosin II-independent cytokinesis in *Dictyostelium*: Its mechanism and implications. *Cell Struct. Funct.* 25:1–10. https://doi.org/10.1247/csf.25.1

Vasta, G.R., H. Ahmed, and E.W. Odom. 2004. Structural and functional diversity of lectin repertoires in invertebrates, protochordates and ectothermic vertebrates. *Curr. Opin. Struct. Biol.* 14:617–630. https://doi.org/10.1016/j.sbi.2004.09.008

Vasta, G.R., C. Feng, N. Gonzalez-Montalban, J. Mancini, L. Yang, K. Abernathy, G. Frost, and C. Palm. 2017. Functions of galectins as "self/non-self"-recognition and effector factors. *Pathog. Dis.* 75:ftx046. https://doi.org/10.1093/femspd/ftx046

Weber, I., G. Gerisch, C. Heizer, J. Murphy, K. Badelt, A. Stock, J.M. Schwartz, and J. Faix. 1999. Cytokinesis mediated through the recruitment of cortexillins into the cleavage furrow. *EMBO J.* 18:586–594. https://doi.org/10.1093/emboj/18.3.586

Weißenbruch, K., J. Grewe, M. Hippler, M. Fladung, M. Tremmel, K. Stricker, U.S. Schwarz, and M. Bastmeyer. 2021. Distinct roles of nonmuscle myosin II isoforms for establishing tension and elasticity during cell morphodynamics. *Elife.* 10:e71888. https://doi.org/10.7554/eLife.71888

West-Foyle, H., P. Kothari, J. Osborne, and D.N. Robinson. 2018. 14-3-3 proteins tune non-muscle myosin II assembly. *J. Biol. Chem.* 293:6751–6761. https://doi.org/10.1074/jbc.M117.819391

West-Foyle, H., and D.N. Robinson. 2012. Cytokinesis mechanics and mechanosensing. *Cytoskeleton.* 69:700–709. https://doi.org/10.1002/cm.21045

Wetterauer, B.W., K. Salger, C. Carballo-Metzner, and H.K. MacWilliams. 1995. Cell-density-dependent repression of discoidin in *Dictyostelium discoideum*. *Differentiation.* 59:289–297. https://doi.org/10.1046/j.1432-0436.1996.5950289.x

Yumura, S., M. Ueda, Y. Sako, T. Kitanishi-Yumura, and T. Yanagida. 2008. Multiple mechanisms for accumulation of myosin II filaments at the equator during cytokinesis. *Traffic.* 9:2089–2099. https://doi.org/10.1111/j.1600-0854.2008.00837.x

Zhang, W., and D.N. Robinson. 2005. Balance of actively generated contractile and resistive forces controls cytokinesis dynamics. *Proc. Natl. Acad. Sci. USA.* 102:7186–7191. https://doi.org/10.1073/pnas.0502545102

Zhou, Q., Y.S. Kee, C.C. Poirier, C. Jelinek, J. Osborne, S. Divi, A. Surcel, M.E. Will, U.S. Eggert, A. Muller-Taubenberger, et al. 2010. 14-3-3 coordinates microtubules, Rac, and myosin II to control cell mechanics and cytokinesis. *Curr. Biol.* 20:1881–1889. https://doi.org/10.1016/j.cub.2010.09.048

Supplemental material
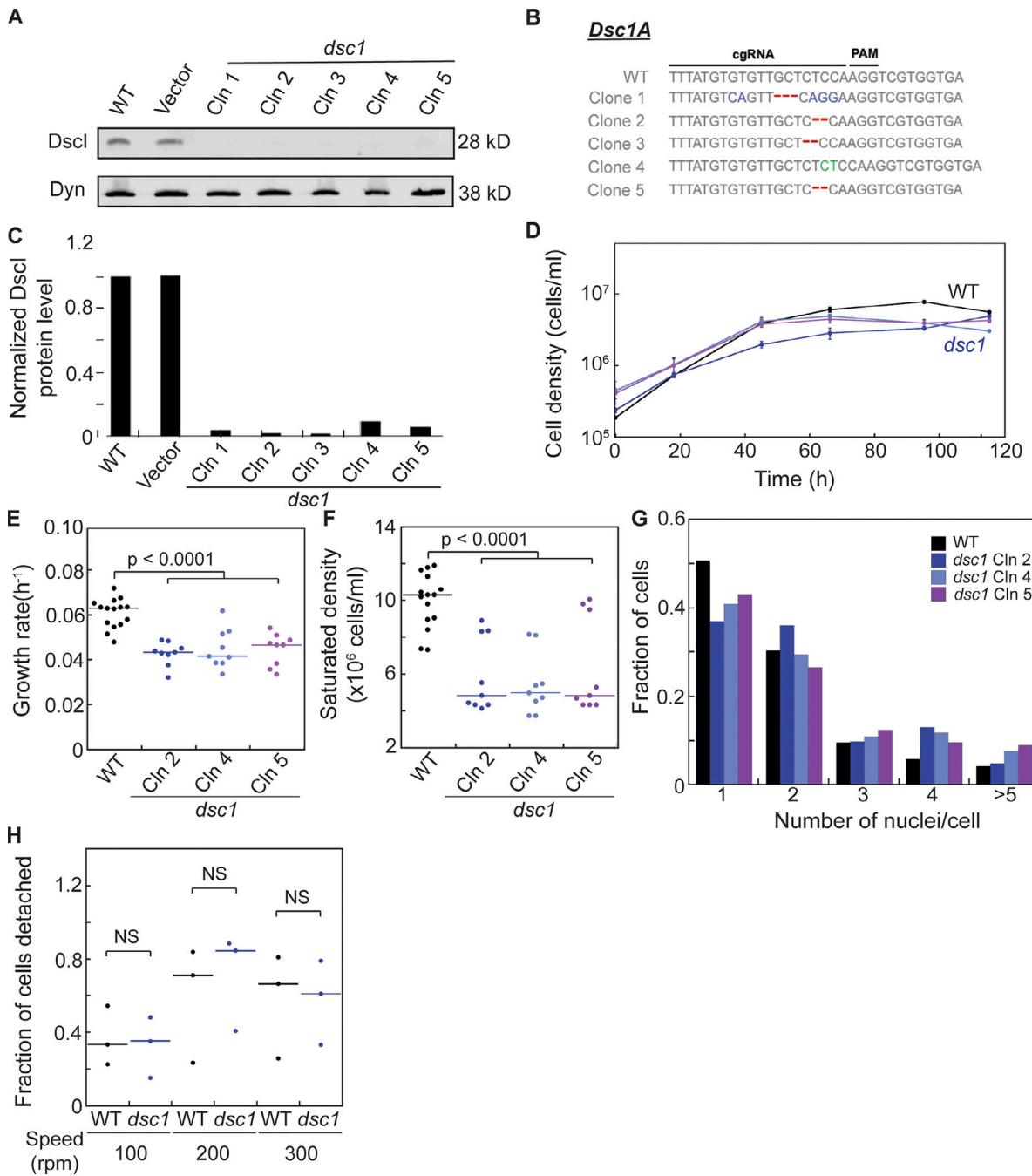
Figure S1. **Cytokinetic defects in *dsc1* null mutants generated in the Ax2 background. (A)** *dsc1* null mutant clones generated in the Ax2 background were verified using Western analysis. Western blot showed absence of DscI protein in all *dsc1* null mutant clones. Dynacortin (Dyn) is provided as a loading control. **(B)** Sequencing analysis confirmed mutations on the *dsc1A* coding genes of *dsc1* mutant clones. Sequences of WT and five separate clones are presented. Nucleotide changes are shown in blue, deletions in red, and insertions in green. **(C)** Quantification of DscI protein level of the Western blot provided in A. Average integrated intensity of each DscI band was background-subtracted and normalized to their corresponding Dyn control band. Each value was then normalized to WT. **(D)** Representative growth curves showed that *dsc1* null mutants in Ax2 background also display mild growth defects in suspension culture. Cell densities, as indicated, were plotted as a function of time. Growth curve for WT (vector control) cell line is shown in black and those for *dsc1* null mutant clones are shown in shades of blue and purple. *dsc1* mutant clone 2,4 and 5 were used for this experiment. *n* = 3 per growth curve, bars represent SEM. **(E)** Growth rates quantified during exponential growth showed mild yet significant defects in growth in different *dsc1* mutant clones. Number of cells analyzed, *n* = 9–15 from three independent experiments. **(F)** *dsc1* mutants generally stopped growing at a significantly lower saturated density as compared to WT control. For E and F, P values were calculated using ANOVA followed by Fisher's LSD test. Number of cells analyzed, *n* = 9–15 from two independent experiments. **(G)** Quantification of the number of nuclei per cell when cells were 3 d in suspension culture. All *dsc1* mutant clones analyzed became more multinucleated compared to WT control. *n* = 2 per cell line with 100–200 cells per cell line quantified per replicate. **(H)** Graph shows quantification of fraction of cells detaching when WT and *dsc1* cells at equal densities were rotated at different speeds on 6-well non-culture-treated plates. Amount of cells detaching was normalized to the seeding cell number, and the ratio of cell detached over total cell number was determined. P values were calculated using ANOVA followed by Fisher's LSD test. Number of samples analyzed, *n* = 3. Source data are available for this figure: SourceData FS1.
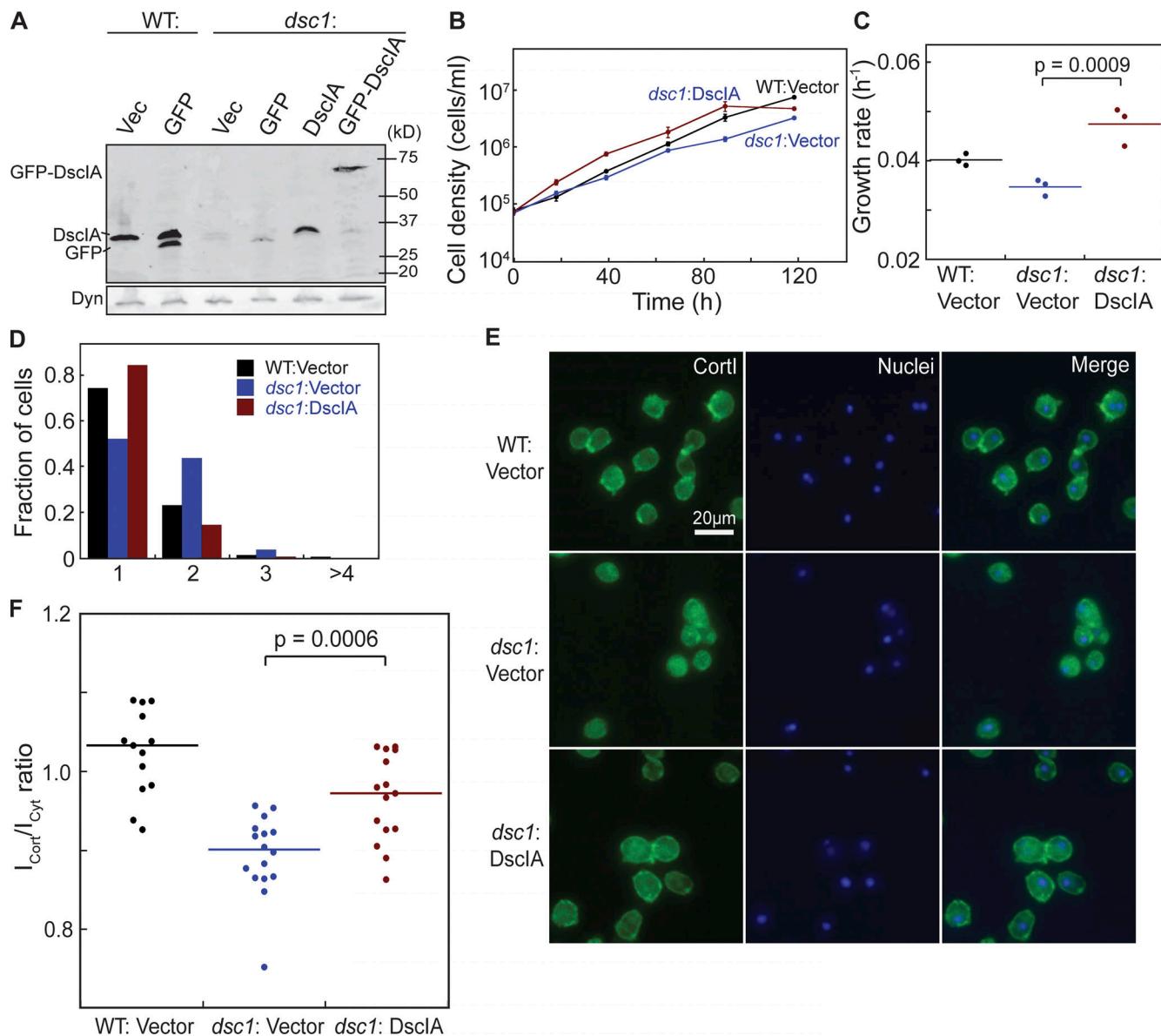
Figure S2. **Exogenous expression of DscIA rescues cytokinetic defects of _dsc1_ null mutants. (A)** Western analysis verified expression of exogenous DscIA and GFP-DscIA in WT and _dsc1_ null background (KAx3 background). **(B)** Representative growth curves in suspension culture revealed that exogenous expression of DscIA rescues growth defect of _dsc1_ null mutants. Cell densities, as indicated, were plotted as a function of time. Growth curve for WT expressing empty plasmid is shown in black; that for _dsc1_ null expressing empty plasmid is shown in blue with round symbols; and that for _dsc1_ null expressing DscIA is shown in blue with square symbols. _n_ = 3 per growth curve, bars represent SEM. **(C)** Growth rates quantified during exponential growth showed an increase in growth in _dsc1_ null complemented cells compared to null cells. P values were calculated using ANOVA followed by Fisher's LSD test. **(D)** Quantification of the number of nuclei per cell when cells were 3 d in suspension culture. **(E and F)** Representative confocal immunofluorescence images of WT and _dsc1_ mutants stained with anti-CortI (green) and Hoescht for nuclei (blue) show that expression of DscIA in _dsc1_ null cells restored the level of CortI at the cortex, quantified in panel F (number of cells analyzed, _n_ = 13–16), back to WT level. P values were derived for ANOVA followed by Fisher's LSD test. Source data are available for this figure: SourceData FS2.
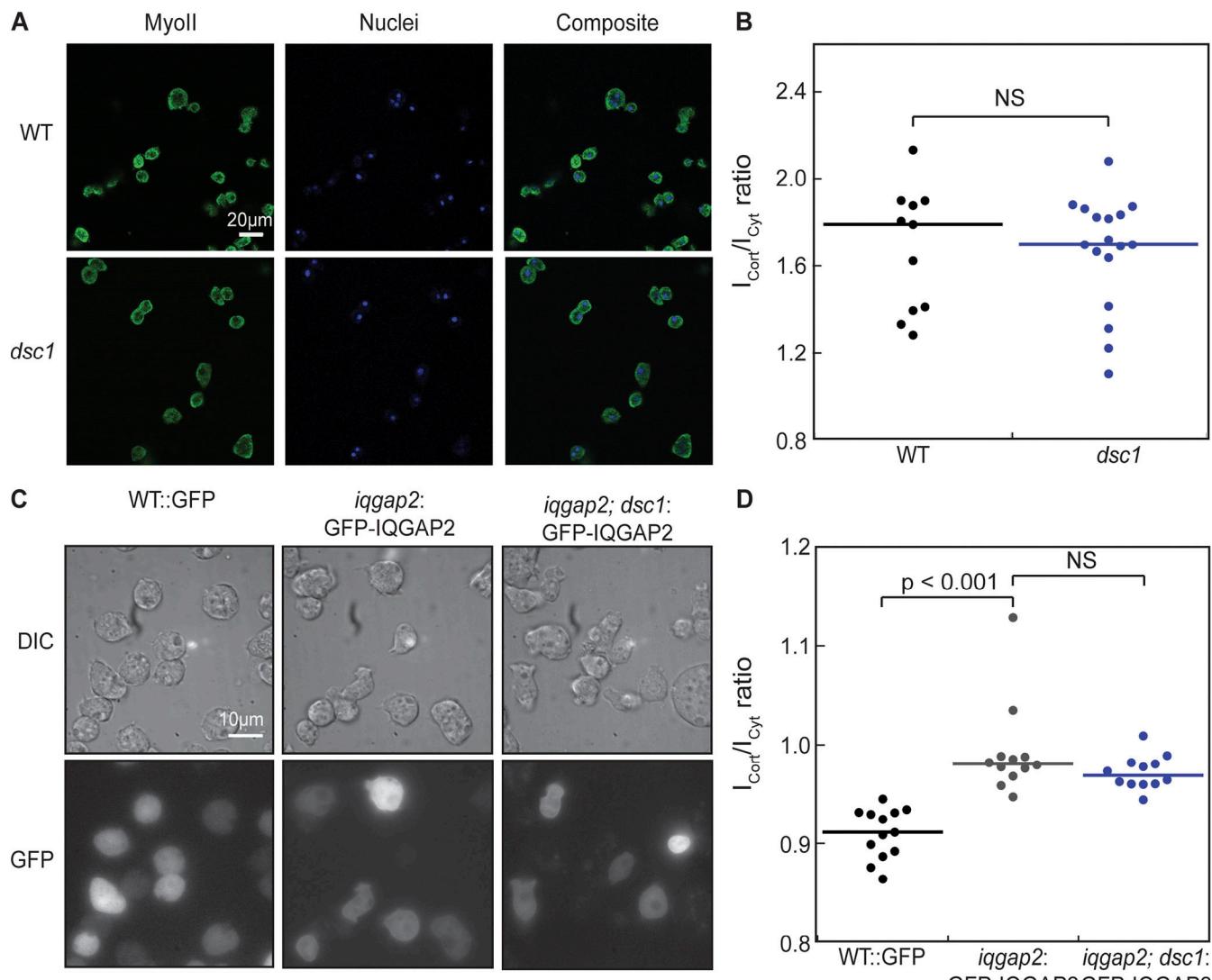
Figure S3. **The absence of DscI in the cell has no effect on the cortical localization of MyoII and IQGAP2. (A)** Representative confocal immunofluorescence images of WT and *dsc1* mutants stained with anti-myoII heavy chain My6 antibody (green) and Hoescht for nuclei (blue) revealed that the amount of MyoII at the cortex is unaffected in the *dscI* mutants. **(B)** Cortical MyoII localization was quantified as the ratio of mean signal intensity at the cortex (I_{cort}) to the mean signal intensity of the cytoplasm (I_{cyt}). No significant difference in this ratio between WT ($n = 11$) and *dsc1* ($n = 17$) cells was present. **(C)** Representative DIC and GFP images of WT cells expressing GFP-alone control, *iqgap2* expressing GFP-IQGAP2, and *iqgap2; dsc1* expressing GFP-IQGAP2 are provided. A thin layer of IQGAP2 is present underneath the membrane in *iqgap2*::GFP-IQGAP2 and in *iqgap2; dsc1* ::GFP-IQGAP2, but not in the GFP-alone cells. **(D)** Quantification of cortical IQGAP2 showed that there was no significance difference in the amount of IQGAP2 at the cortex between cells lacking DscI expression and positive control. All P values were derived for ANOVA followed by Fisher's LSD test. Number of cells analyzed, $n = 12$–13.
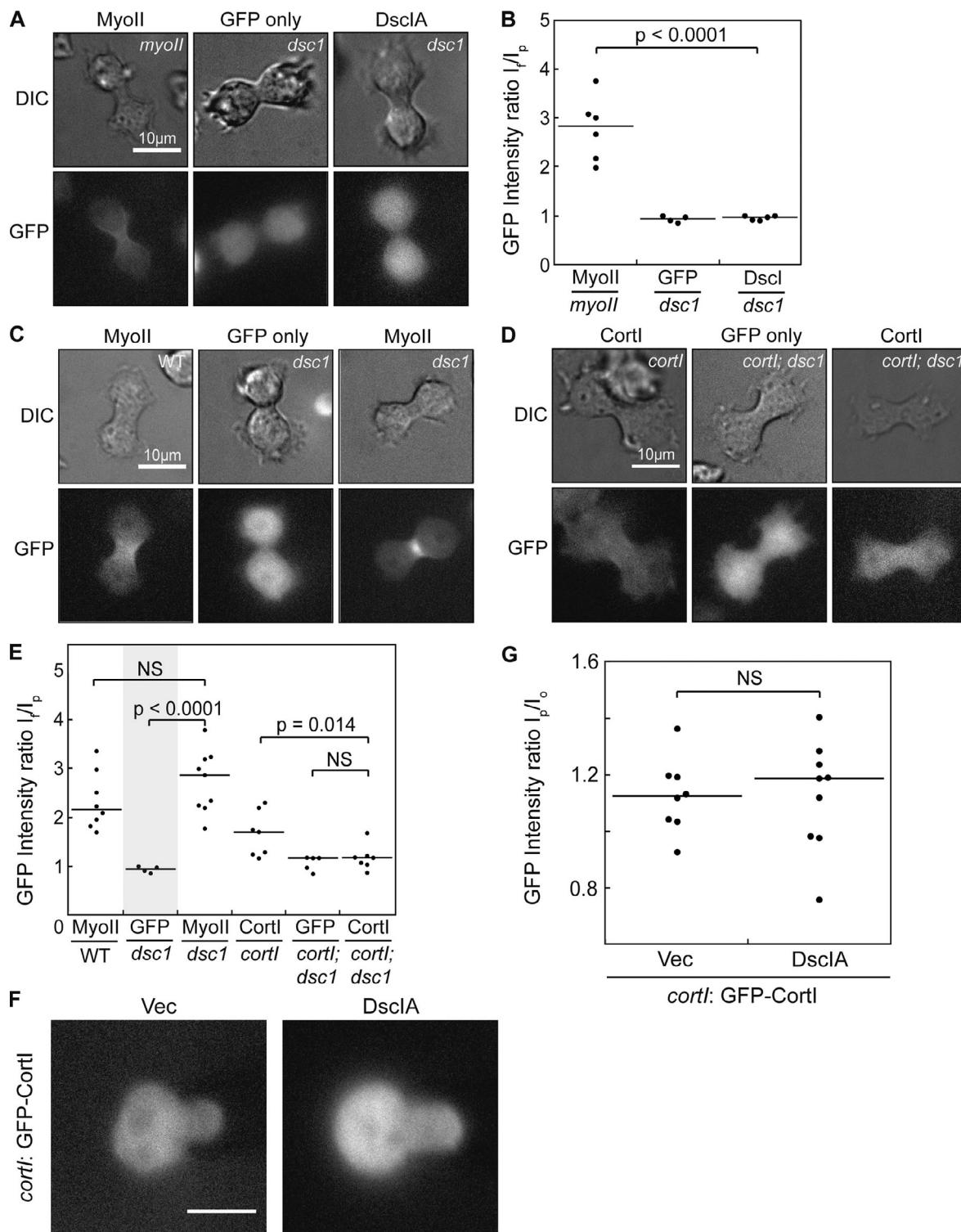
Figure S4. DscI facilitates CortI's cleavage furrow accumulation. (A) DIC and GFP images show localization of GFP-MyoII, GFP alone, and GFP-DscIA as cells form cleavage furrows during cytokinesis (from left to right). GFP-MyoII serves as a positive control. **(B)** The ratio of the background-corrected mean GFP signal intensity of both sides of the furrow (I_f) to that of both of the poles (I_p) was measured. Number of cells analyzed, n = 4–6 from three independent experiments. **(C and D)** GFP images show accumulation of GFP-CortI and GFP-MyoII at the cleavage furrow in cells with and without DscI. **(E)** Quantification of I_f/I_p ratio for GFP-CortI and GFP-MyoII signals at the cleavage furrows as cells of different genetic backgrounds divide. I_f/I_p ratio for vector expression in *dsc1* cells (shaded) is reproduced from B for direct comparison. All P values were derived by ANOVA followed by Fisher's LSD test. **(F)** GFP images show localization of GFP-CortI in *cortI* null–complemented cells with DscIA overexpression as these cells were aspirated by micropipette. Number of cells analyzed, n = 4–9 from two independent experiments. Vec, vector. **(G)** The degree of mechanoresponsiveness of GFP-tagged proteins was quantified as the GFP intensity ratio (I_p/I_o) of the cortex inside the pipette (I_p) to the cortex on the opposite side of the cell (I_o). P values were derived from ANOVA followed by Fisher's LSD test. Number of cells analyzed, n = 8–9 from two independent experiments.
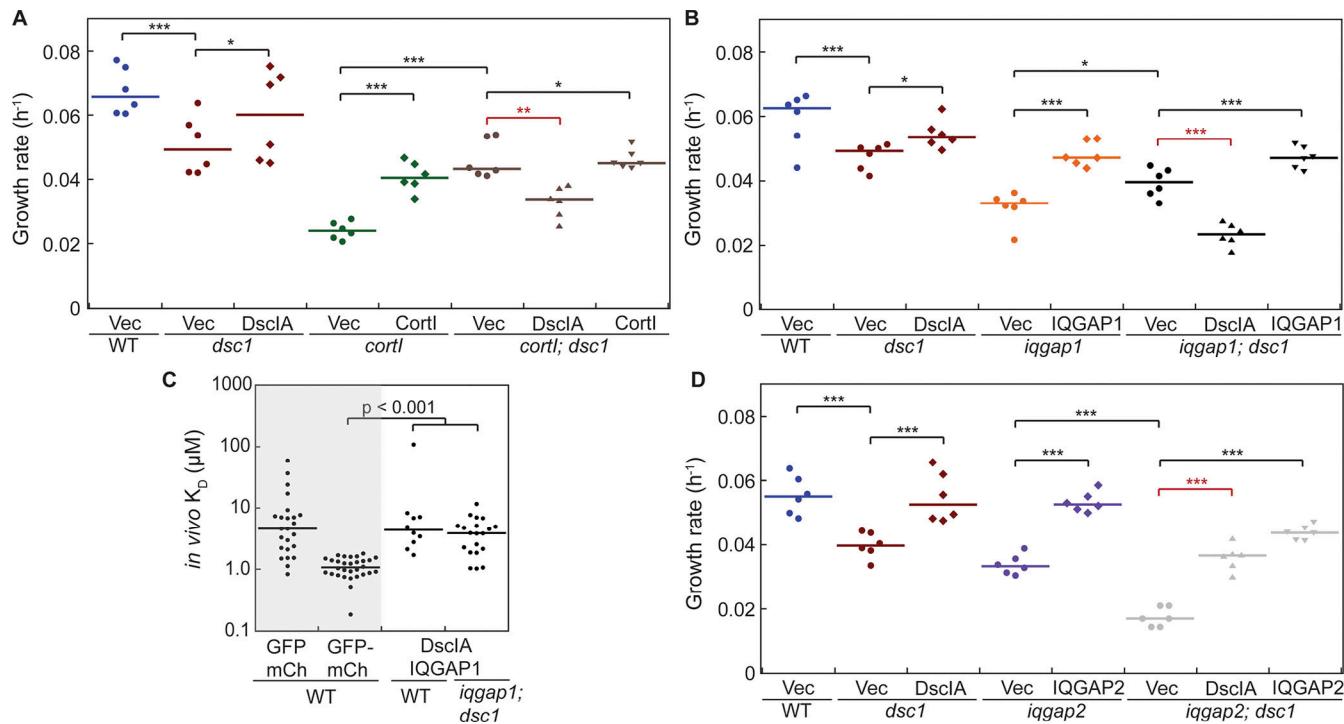
Figure S5. **DscIA has antagonistic genetic interactions with CortI and IQGAP1 and synergistic genetic interactions with IQGAP2. (A)** Quantification of growth rates during exponential growth in suspension of WT (blue), *dsc1* (red) and *cortI* (green) single mutants, and double mutant (brown) expressing empty plasmids together with their corresponding complemented backgrounds. Expression of DscIA and CortI had opposite effects on growth of *cortI; dsc1* double mutant cells. Exogenous expression of DscIA in the absence of CortI was deleterious to growth. Exogenous expression of DscIA rescued the growth defect of *dsc1* null, while CortI partially rescued the growth defect of *cortI* null. Number of cell samples, *n* = 6 from two independent experiments. **(B)** Quantification of growth rates during exponential growth in suspension of WT (blue), *dsc1* (red) and *iqgap1* (orange) single mutants, and double mutant (black) expressing empty plasmids together with their corresponding complemented backgrounds. Exogenous expression of DscIA in the absence of IQGAP1, similar to that of CortI, was also deleterious to growth of *iqgap1; dsc1* cells. Exogenous expression of IQGAP1 rescued growth of the double mutant cells. Number of cell samples, *n* = 6 from two independent experiments. **(C)** FCCS measurement of in vivo K_D values demonstrated that DscIA and IQGAP1 do not detectably interact in the cytoplasm in either the WT or in the *iqgap1; dsc1* complemented backgrounds. Positive and negative controls (shaded) in WT background are reproduced from Fig. 7 C. Compared to the negative control, the P values of the interactions in the WT background was 0.64 and in the *iqgap1; dsc1*-complemented background was 0.16. P values were derived from an ANOVA followed by Fisher's LSD test. Number of cells analyzed, *n* = 10–30 from two independent experiments. **(D)** Quantification of growth rates during exponential growth in suspension of WT (blue), *dsc1* (red) and *iqgap2* (purple) single mutants, and double mutant (gray) expressing empty plasmids together with their corresponding complemented backgrounds. Exogenous expression of DscIA and IQGAP2 rescued the growth of *iqgap2; dsc1* double mutant cells, returning growth to the single mutant levels. All growth rate values in these experiments are detailed in Table S2. All P values were derived by ANOVA followed by Fisher's LSD test (*, P < 0.05; **, P < 0.001; ***, P < 0.0001). Number of cell samples, *n* = 6 from two independent experiments.

Video 1. **Video of a dividing WT (KAx3) cell.** Each frame was collected every 2 s with a 40× (NA 1.30) oil objective and imaged by DIC using an Olympus IX71 microscope. Playback speed is 10 frames per second.

Video 2. **Video of a dividing dsc1 null cell.** Each frame was collected every 2 s with a 40× (NA 1.30) oil objective and imaged by DIC using an Olympus IX71 microscope. Playback speed is 10 frames per second.

Video 3. **Video of a dividing dsc1:GFP-DscIA cell.** Each frame was collected every 5 s with a 40× (NA 1.30) oil objective and imaged by DIC using an Olympus IX71 microscope. Playback speed is 3 frames per second.

Video 4.   **Video of a dividing iqgap2 null cell.** Each frame was collected every 2 s with a 40× (NA 1.30) oil objective and imaged by DIC using an Olympus IX71 microscope. Playback speed is 10 frames per second.

Video 5.   **Video of a dividing iqgap2; dsc1 null cell.** Each frame was collected every 2 s with a 40× (NA 1.30) oil objective and imaged by DIC using an Olympus IX71 microscope. Playback speed is 10 frames per second.

Provided online are two tables. Table S1 is a summary of all *D. discoideum* cell strains used in this study. Table S2 lists growth rates of background and null-complemented cell lines used in genetic interaction assays. Absolute growth rates in h^{-1} are shown.